Comparative Study of CCPS Based on Permanent Magnet and Electrically Excited HIA for Selecting Rational Topological Structure

Longjian LIU, Kexun YU, Xianfei XIE, and Zhijian LIU

***Abstract*—In order to facilitate the selection of an optimal topological structure for rational pulsed capacitor charging power supplies (CCPS), this paper presents a comparative analysis of CCPS based on permanent magnet excited (PME) and electrically excited (EE) homopolar inductor alternators (HIA). The findings indicate that the *d*-axis transient inductance of the PME HIA is marginally greater than that of the EE HIA, a result that contradicts initial expectations. Notably, the PME HIA does not require consideration of transient flux variations, whereas the EE HIA does. The study establishes relationships among the enhancement of charge performance, efficiency, capacitance, frequency, and field winding (FW) resistance. It is observed that as capacitance, frequency, and FW resistance increase, there is a corresponding improvement in charge performance. The equipotential line representing the enhancement of charge performance approximates an inverse proportional function, suggesting that if the product of FW resistance and capacitance, or the product of FW resistance and frequency, remains constant, the improvement in charge performance will also be constant. Furthermore, it is noted that as capacitance and frequency increase, the improvement in efficiency diminishes, which is contrary to the trend observed in charge performance. To comprehensively evaluate the enhancement of charge performance and efficiency, a weighted function is proposed. This function aids in the selection of a rational topological structure for CCPS, distinguishing between those based on PME HIA and those based on EE HIA. Based on the results derived from the weighted improvement analysis, appropriate topological structures for CCPS can be identified according to varying capacitance, frequency, and FW resistance. Specifically, when the product of capacitance and FW resistance, or the product of frequency and FW resistance, is substantial, the PME HIA is recommended; conversely, the EE HIA is preferred in other scenarios.**

***Index Terms*—Average-value model, capacitor charge power supply, charge performance, electrically excited HIA, Permanent magnet excited HIA.**

I. Introduction

THE capacitor charging power supply (CCPS) plays a crucial role in national defense and advanced technology applications [1]−[9]. Notably, the high-current, high-voltage pulsed CCPS based on homopolar inductor alternator (HIA) represents a promising type of pulsed power supply (PPS) for use in innovative equipment. To facilitate the generation of repetitive pulses, the inertial energy storage capabilities of HIA are employed. The advantages of HIA include high reliability, elevated power density, and significant energy storage density. A substantial body of research addressing optimal design, efficiency, loss analysis, and testing of this type of PPS is documented in [10]−[19]. Furthermore, considerable efforts have been dedicated to the development of modeling techniques for this type of PPS, as discussed in [10]−[11], [17]−[19]. Various analytical models have been proposed, including the voltage behind resistance (VBR) model [18]−[19], the average-value model (AVM) [17], and the inductance matrix model [11].

A compensatory HIA was proposed in [20]−[23], which further increased the power density of this type of machine. However, the compensation windings require a substantial amount of space. In [24], a pulsed CCPS based on high-temperature superconducting excited (HTSE) HIA is introduced. Simulation results indicate that HTSE HIA exhibits significantly higher power density and efficiency compared to conventional HIA, thereby enhancing the performance of this type of PPS. Despite the favorable performance of HTSE HIA, its application in practical engineering is constrained by the high costs and the extended cooling period required for the superconducting tape.

The electrically excited (EE) HIA experience excitation loss due to their dependence on the current of the field winding (FW) to generate a magnetomotive force (MMF). Furthermore, the dynamic process of establishing the excitation magnetic field is protracted, often extending to the second level, owing to the considerable time constant associated with the FW. This dynamic alteration of the excitation magnetic field results in continuous fluctuations in the amplitude of the HIA's no-load back electromotive force (EMF) throughout the process. Con-

Manuscript received October 07, 2024; revised December 24, 2024; accepted February 16, 2025. Date of publication March 30, 2025; date of current version February 28, 2025. This work was supported in part by National Key Research and Development Program of China under the grant 2022YFB2703500, Key Research and Development Program of Yunnan Province under the grant 202303AA080002, Foundation of State Key Laboratory of Advanced Electromagnetic Technology under the Grant AET2024KF013, Foundation of Yunnan Fundamental Research Projects under the Grant 202301AS070055, and Foundation of KUST under the Grant KKZ3202404099. *(Corresponding author: Zhijian Liu.)*

L. Liu and Z. Liu are with the Faculty of Electric Power Engineering, Kunming University of Science and Technology, Kunming, 650500, China (e-mail: liulongjian001@yeah.net; 12310010@kust.edu.cn).

K. Yu and X. Xie are with the State Key Laboratory of Advanced Electromagnetic Technology, Huazhong University of Science and Technology, Wuhan, 430074, China (email: yukexun@hust.edu.cn; xiexianfei@hust.edu.cn).

Digital Object Identifier 10.24295/CPSSTPEA.2025.00005

sequently, the overall efficiency of the system is diminished, as the no-load iron core losses consume a portion of the energy stored in the rotor of the HIA during the excitation establishment stage, given that the no-load back EMF remains relatively stable prior to the charging of the capacitor. Additionally, the transient voltage of the HIA experiences a rapid decline due to the excessively swift transient flux attenuation during the charging process. This phenomenon significantly impacts the charging performance [18]. Moreover, if the excitation time constant [25] is increased by enlarging the cross-sectional area of the winding, it may lead to the FW occupying an excessive amount of space, thereby resulting in an increase in the size and weight of the HIA.

To address the challenges previously identified, a CCPS utilizing PME HIA has been proposed in our prior research, which is characterized by the absence of FW and excitation time constant [26]. To facilitate the selection of an appropriate topological structure for the CCPS, a comprehensive analysis of the CCPS based on PME HIA is warranted. This is particularly important given that the variations in transient flux between PME HIA and EE HIA, as well as the differences in AVM between CCPS configurations based on EE HIA and PME HIA, have not been thoroughly examined. Furthermore, a comparative analysis of charge performance and efficiency between the CCPS based on EE HIA and PME HIA remains to be investigated. Detailed explanations of these aspects are provided below.

Firstly, while our previous study has demonstrated that the equivalent inductance values in the AVM differ between the PME HIA and the EE HIA, the extent of this relationship has not been thoroughly examined in [26]. The equivalent inductance value significantly influences the charge performance of CCPS. Generally, the equivalent inductance of PME HIA is expected to be considerably larger than that of EE HIA, primarily due to the substantial reduction of the *d*-axis transient inductance in EE HIA caused by the effects of the FW. Consequently, from the perspective of equivalent inductance, the power density of CCPS utilizing PME HIA may be significantly lower than that of EE HIA. Conversely, for EE HIA, the transient flux attenuation may lead to a dramatic reduction in power density. Thus, in this context, the power density of CCPS based on PME HIA could be considerably higher than that of EE HIA. Given this analysis, the relationship between the power densities of CCPS based on PME HIA and EE HIA remains ambiguous. In scenarios where the charge time is short and the FW resistance is minimal, the effects of transient flux attenuation are negligible; under these conditions, the power density of CCPS utilizing EE HIA may exceed that of PME HIA. Conversely, when the charge time is prolonged and the FW resistance is substantial, the effects of transient flux attenuation become pronounced, potentially resulting in a higher power density for CCPS based on PME HIA compared to EE HIA. Therefore, it is imperative to conduct a careful comparison of the charge performance of CCPS based on PME HIA and EE HIA, and to identify the critical values of charge time and FW resistance at which the charge performances of both

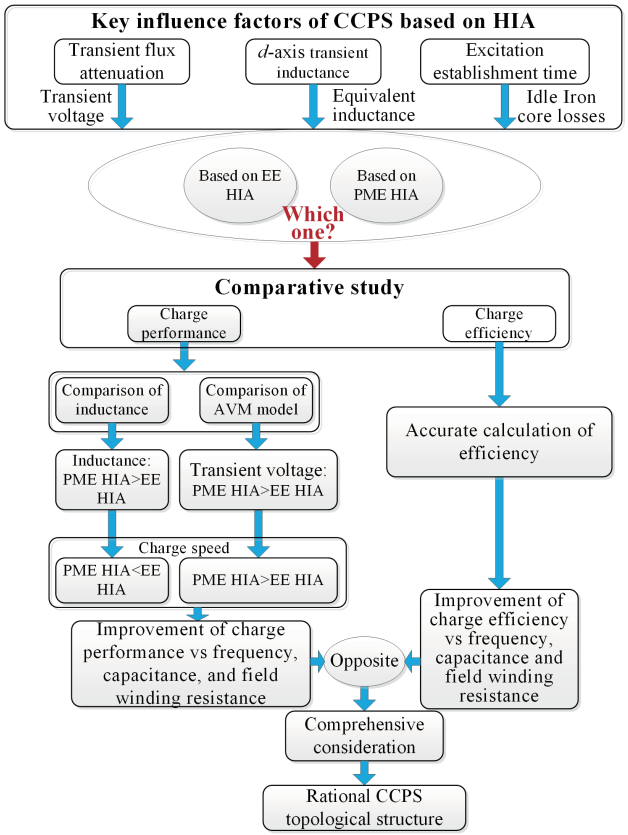

Fig. 1. The flow chart of this paper.

systems are equivalent. To facilitate a more intuitive comparison of charge performance, it is essential to investigate the relationship between the equivalent inductance values of PME HIA and EE HIA, as well as to compare the AVMs of CCPS based on PME and EE HIAs.

Secondly, regarding the issues of efficiency, the efficiency of the CCPS is related to both the duration of the charging time and the resistance of the FW. Specifically, a longer charging time results in a smaller proportion of energy losses attributed to no-load iron core losses during the excitation establishment stage, thereby enhancing the overall efficiency of the CCPS. Consequently, this leads to a reduced efficiency improvement for the CCPS when comparing the PME HIA with the EE HIA. It is evident that the trends in the improvement of charging performance and efficiency are inversely related. Additionally, the resistance of the FW affects the charging voltage, which in turn influences the efficiency of the system. Therefore, when selecting the topological structure of the CCPS between PME HIA and EE HIA, it is essential to consider both charging performance and efficiency in a comprehensive manner. The charging time is directly proportional to the capacitance and frequency; thus, the precise values for the improvements in performance and efficiency of the CCPS based on PME HIA compared to EE HIA must be calculated meticulously for varying capacitance, frequency and FW resistance. Once the relationships between the improvements in charging performance, efficiency, capacitance, frequency and FW resistance are established, the optimal topological structure of the CCPS

can be determined.

In order to address the two issues presented above, this paper conducts a comparative study of CCPS based on PME and EE HIA systems. The flowchart illustrating the structure of this paper is presented in Fig. 1. To facilitate comparison, the sizes of the PME HIA and EE HIA are kept constant, and the amplitudes of the no-load back EMF are equal. The organization of the paper is as follows: First, the fundamental structure and operational principles of the CCPS based on PME HIA are briefly outlined. Subsequently, a comparative analysis of the parametric properties of the PME and EE HIAs is conducted, focusing on the no-load magnetic field, back EMF, and transient inductance. Furthermore, considering the transient flux attenuation, the AVMs of the CCPS based on PME and EE HIAs are compared and analyzed. Finally, the charging performance and efficiency of the pulsed CCPS based on PME and EE HIAs are evaluated. The improvements in charging performance relative to capacitance, frequency and FW resistance, as well as the enhancements in charging efficiency concerning capacitance, frequency and FW resistance, are presented. Based on the simulation results, a comprehensive consideration is proposed for selecting an optimal topological structure for CCPS, comparing the configurations based on PME HIA and EE HIA.

The research presented in this paper demonstrates that the time required for the PME HIA is significantly less than that needed to generate the excitation magnetic field of the EE HIA. This efficiency is attributed to the PME HIA's ability to rapidly establish back EMF through mechanical magnetic adjustment. Consequently, the PME HIA exhibits lower energy consumption compared to the EE HIA concerning no-load iron core losses. Furthermore, the absence of transient flux attenuation, a phenomenon unique to EE HIAs, ensures that charging performance remains unaffected by transient flux reduction. The findings indicate that the *d*-axis transient inductance of the PME HIA is slightly greater than, rather than substantially greater than, that of the EE HIA, which does not align with initial expectations.

II. Block Diagram and Principle of CCPS

The comparison of two topological structures of the pulsed CCPS based on the PME HIA and the EE HIA is illustrated in Fig. 2. In the case of the PME HIA, a magnetic modulator ring (MMR), composed of a magnetic permeable material, is arranged coaxially with the casing outside the permanent magnet (PM). The axial position of the MMR is regulated and adjusted by an actuator [27]–[28].

The function of the MMR is delineated as follows. By varying the position of the MMR, the HIA can operate under two distinct conditions. As illustrated in Fig. 3(a), when the MMR is positioned at a considerable distance from the PM, its influence on the magnetic field is minimal. Consequently, the air-gap magnetic flux density is substantial, resulting in a significant induced voltage within the armature winding. Under these circumstances, the HIA is capable of charging the capacitor via the rectifier. Conversely, when the HIA is required to operate in an idling condition, the MMR aligns with the PM, as depicted in Fig. 3(b).

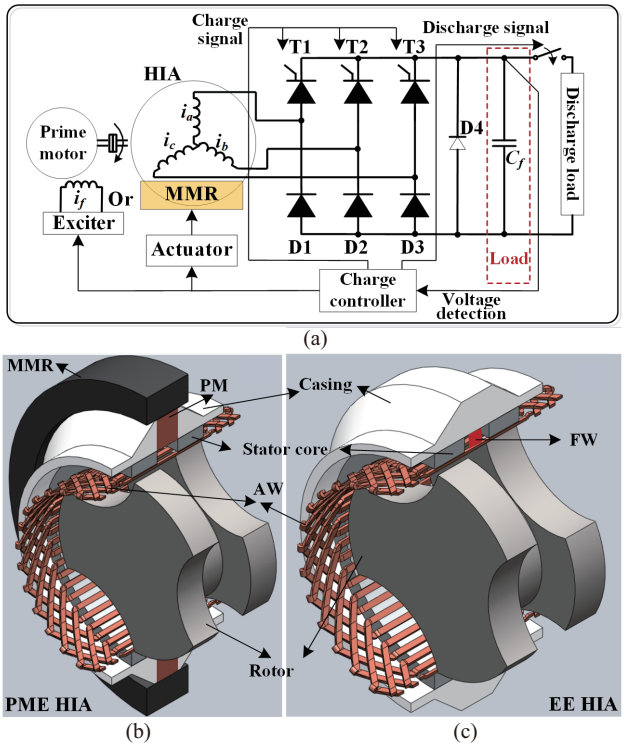

Fig. 2. (a)The comparison of two topological structures between CCPS based on PME HIA and EE HIA, (b) PME HIA structure, (c) EE HIA structure.

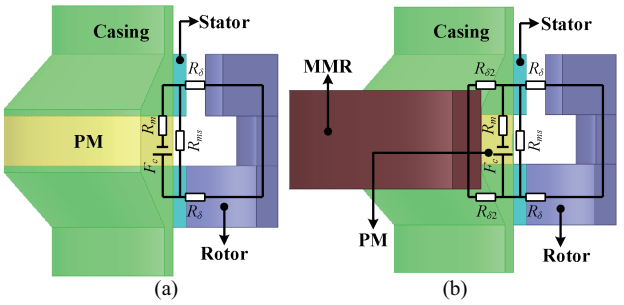

Fig. 3. The magnetic circuit model of the PME HIA. (a) The magnetic adjusting ring is in the open circuit state position, (b) The magnetic adjusting ring is in the short circuit state position.

In this scenario, the MMF generated by the PM is effectively short-circuited by the MMR, leading to a markedly reduced air-gap magnetic flux density. As a result, the no-load iron core losses during idling are also minimized. To further mitigate these no-load iron core losses, it is imperative that the air-gap length between the HIA casing and the MMR be minimized.

The sequence diagram for CCPS based on the PME or EE HIA is shown in Fig. 4. Taking the PME HIA as example, the system workflow is as follows:

1) Initially, at time 0, the actuator modifies the MMR's position to short-circuit the PM's MMF. At this point, the HIA's no-load magnetic field is extremely low, which can effectively reduce the HIA's iron core loss when it is not loaded. From time 0 to t_{begin}, the HIA rotor is speeded up from zero to its maximum operating speed by means of the prime mover.

2) From time t_{begin} to $t_{begin}+t_{MMR}$, the actuator controls the

MMR's position to keep it away from the PM when the capacitor has to be charged. The HIA air gap can create a normal-amplitude magnetic field, and the back EMF is emitted in the winding.

3) At time of $t_{begin}+t_{MMR}$, the rectifier bridge's thyristors are activated simultaneously, and the capacitor is then charged via the rectifier bridge. The HIA rotor's inertial energy storage is transformed into electrical energy on the capacitor during charging.

4) At time of $t_{begin}+t_{MMR}+t_{charge}$, after the voltage on the capacitor reaches the predetermined level, the rectifier bridge's thyristors are then turned off and the discharge circuit switch is activated, releasing the electric energy stored in the capacitor into the pulse load instantaneously.

Repeat the above processes 3) and 4) to achieve a repetition of charge and discharge pulses. At time of t_{end}, when a charge-discharge pulse beam is completed, making the MMR align with the PM, and steps 1) and 2) are executed, and steps 3) and 4) are repeated again to achieve a plurality of charge-discharge pulse beams.

For the EE HIA, for step 2), the magnetic field is established by applying the field current.

III. Comparisons of No-load Magnetic Field and Back EMF of the Machine

A. Comparison of Magnetic Circuit Models

The magnetic circuit model of the mechanically modulated PME HIA is detailed in [27]–[28]. For analytical purposes, the magnetic circuit model disregards the MMF drop in ferromagnetic materials. This paper focuses on two specific states, as illustrated in Fig. 3. In state (a), the MMR is positioned at an open-circuit configuration, while in state (b), the MMR is in a short-circuited configuration.

When the MMR is at open-circuit position, according to the magnetic circuit model, the expression of the air-gap MMR drop of the HIA is:

$$F_\delta = F_c \frac{2R_\delta R_{ms}}{2R_\delta + R_{ms}} \Bigg/ \left(\frac{2R_\delta R_{ms}}{2R_\delta + R_{ms}} + R_m \right) \tag{1}$$

When the MMR is at short-circuited position, according to the magnetic circuit model, the expression of the air-gap MMR drop of the HIA is:

$$F_\delta = F_c \frac{\left(\dfrac{\dfrac{2R_\delta R_{ms}}{2R_\delta + R_{ms}} 2R_{\delta 2}}{\dfrac{2R_\delta R_{ms}}{2R_\delta + R_{ms}} + 2R_{\delta 2}} \right)}{\left(\left(\dfrac{\dfrac{2R_\delta R_{ms}}{2R_\delta + R_{ms}} 2R_{\delta 2}}{\dfrac{2R_\delta R_{ms}}{2R_\delta + R_{ms}} + 2R_{\delta 2}} \right) + R_m \right)} \tag{2}$$

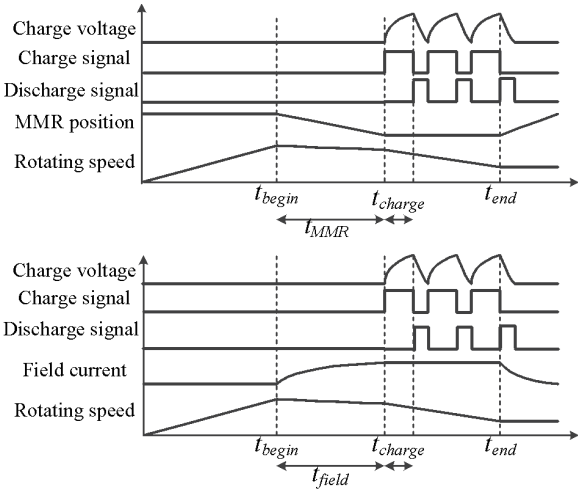

Fig. 4. The sequence diagram for CCPS based on the PME or EE HIA.

In (1) and (2), R_δ, R_{ms}, R_m and $R_{\delta 2}$ are the air-gap magneto resistance, leakage circuit magneto resistance, PM magneto resistance and MMR air-gap magneto resistance respectively. F_c is the MMF of the PM. The calculation methods of each magneto resistance and MMF can be referred to the methods in [29], and the specific calculation formulas are shown in the Appendix A.

The magnetic circuit model of the EE HIA exhibits similarities to that of the PME HIA when the MMR is in the open-circuit position. However, a key distinction lies in the nature of the MMF source. In the case of the PME HIA, the MMF source is represented by a magnetically permeable casing rather than a PM. Additionally, the magnetic resistance in this configuration is considered negligible.

B. Comparison of Air-Gap Magnetic Fields

The calculation expression of the air-gap magnetic flux density of the mechanically modulated PME HIA is:

$$B_\delta = \frac{F_\delta}{2} \lambda_\delta (\theta_r) \tag{3}$$

where F_δ is the MMF drop across the air gap, $\lambda(\theta_r)$ is the magnetic permeance waveform function of the air gap, and θ_r is the electrical angle of the rotor position.

The waveform of the no-load air-gap radial magnetic flux density, as obtained through finite element simulation, is presented in Fig. 5. The key structural parameters of the HIA utilized in the simulation are detailed in Table I. It is observed that when the MMR is positioned at the short-circuit state, the amplitude of the air-gap magnetic flux density is relatively low, approximately 0.2 T. Conversely, when the MMR is at the open-circuit position, the amplitude of the air-gap magnetic flux density increases to about 1.2 T. Given that the iron core loss is proportional to the square of the magnetic flux density, it can be inferred that the no-load iron core loss of the machine will significantly decrease when the MMF of the PM is short-circuited by the MMR. Fig. 5 also illustrates the air-gap magnetic flux

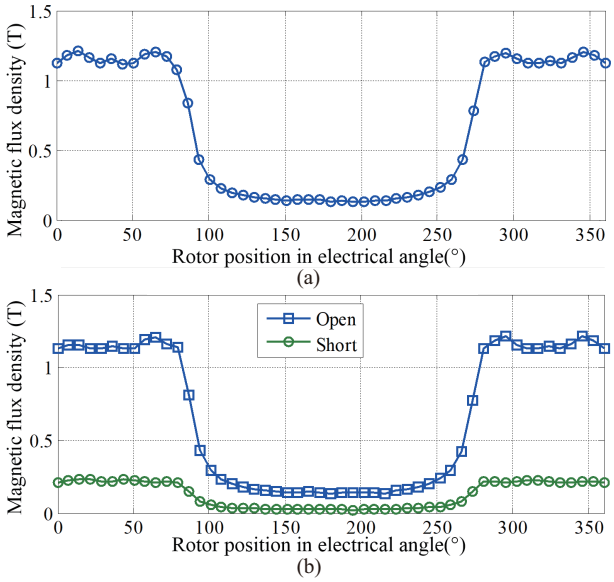

Fig. 5. Comparison of the no-load air-gap magnetic flux density distribution by finite element simulation. (a) EE HIA, (b) PME HIA.

TABLE I
KEY STRUCTURE PARAMETERS OF HIA

Symbol	Parameter	Value
D	Rotor diameter	106 mm
D_i	Stator core inner diameter	110 mm
D_o	Stator core outer diameter	126 mm
p	Pole pair number	3
D_{shell}	Outer diameter of magnet	165 mm
l_m	Length of magnet	15 mm
l	Stator length	18.5 mm
l_c	MMR length	30 mm
h	Rotor slot depth	20 mm
q	Slot number per pole per phase	3
N	Armature winding series turn number per phase	9
δ	Air-gap length	2 mm
δ_2	Air-gap length of modulator	0.25 mm
D_{shaft}	Rotor shaft diameter	65 mm

density for the EE HIA, revealing that the two configurations exhibit essentially identical characteristics. From the aforementioned results, it is evident that the no-load air-gap magnetic flux density of the PME HIA cannot be reduced to zero during idle operation, indicating the presence of no-load iron core loss in this state. In contrast, for the EE HIA, when the excitation is null, the theoretical no-load iron core loss is zero.

C. Comparison of the No-load Line-to-Line Back EMF of the HIA

The waveform of the no-load back EMF for the HIA, as obtained through finite element simulation, is presented in Fig. 6. The structural parameters of the HIA utilized in the simulation are detailed in Table I. Additionally, Table II illustrates the simulation results for the RMS value of the no-load line-to-line back EMF. It is evident that the waveforms exhibit a high degree of similarity.

It can also be seen that when the modulator is at the short-circuit position, the no-load back EMF is small, and

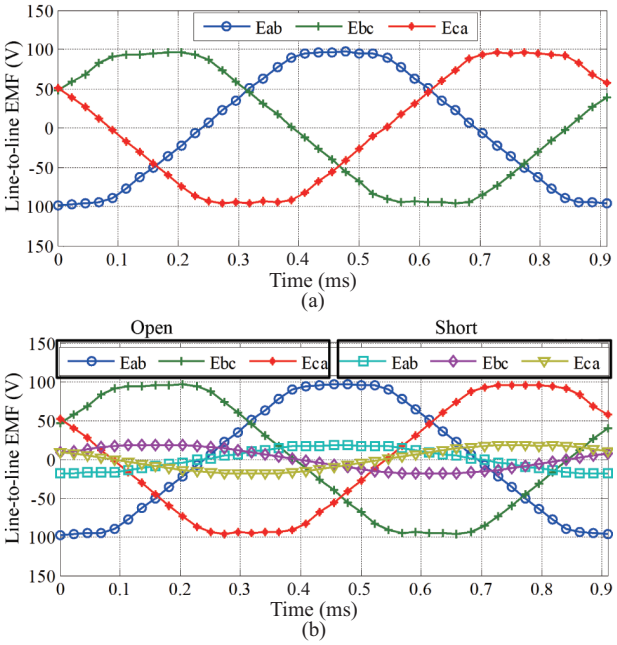

Fig. 6. Comparison of the line-to-line back-EMF waveform by finite element simulation. (a) EE HIA, (b) PME HIA.

TABLE II
ELECTROMAGNETIC PERFORMANCE PARAMETERS OF HIA

Excitation mode	EE	PME
Rated rotating speed	22000 r/min	22000 r/min
RMS value of line-to-line back EMF	68 V	68 V
FW resistance	2 Ω	-
FW inductance	90 mH	-
Reference [30]		
d-axis transient inductance	0.0103 mH	0.0111 mH
q-axis transient inductance	0.0152 mH	0.0152 mH
Inductance matrix method		
d-axis transient inductance	0.0103 mH	0.0127 mH
q-axis transient inductance	0.016 mH	0.016 mH

the RMS value is about 18 V. When the modulator is at the open-circuit position, the amplitude of the no-load line-to-line back EMF is about 96 V, and the RMS value is about 68 V.

IV. COMPARISON OF TRANSIENT INDUCTANCE PARAMETERS OF HIAS

A. d-axis Transient Inductance

The equivalent circuits for the d-axis transient inductance parameters of the PME and EE HIAs are shown in Fig. 7. For EE HIAs, the d-axis transient inductance is calculated as follows:

$$L_d^{'} = L_\sigma + \frac{L_{md} L_{f\sigma}}{L_{md} + L_{f\sigma}} \tag{4}$$

where L_σ is the leakage inductance of the armature winding, and L_{md} is the d-axis armature reaction inductance, which is calculated as follows [30]–[31]:

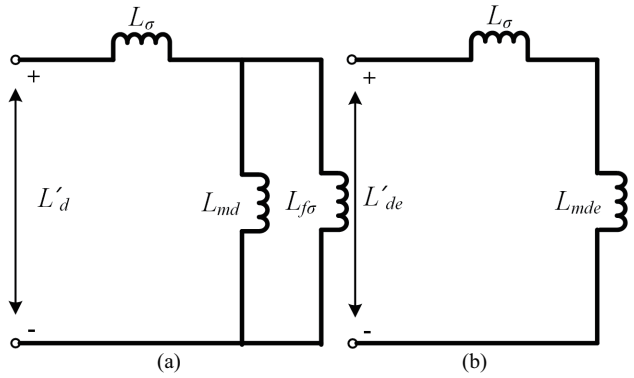

Fig. 7. The equivalent circuit for *d*-axis transient inductance parameter. (a) EE HIA, (b) PME HIA.

$$L_{md} = \frac{6\mu_0 D_i l_{ef}}{\delta \pi k_\delta} \left(\frac{N k_N}{p}\right)^2 \left(\lambda^*_0 + \frac{\lambda^*_2}{2}\right) \tag{5}$$

where l_{ef} is the effective length of the stator, k_N is the winding coefficient, k_δ is the Carter's coefficient of the stator, μ_0 is the vacuum permeability, and λ^*_0 and λ^*_2 represents the per-unit values of the DC component and the secondary component of air-gap permeance, respectively.

$L_{f\sigma}$ is the leakage inductance of the FW in the stator side, and is calculated as follows:

$$L_{f\sigma} = \frac{3}{2} k_f^2 \, L_f - L_{md} \tag{6}$$

The variable k_f denotes the converted coefficient for inductance between the rotor side and the stator side, with the calculation formula provided below:

$$k_f = \frac{4 N k_N}{\pi p N_f} \frac{\left(\lambda^*_0 + \frac{\lambda^*_2}{2}\right)}{\lambda^*_1} \tag{7}$$

where N_f is the number of turns of the FW, and λ^*_1 is the per-unit value of the fundamental component of the air-gap permeance.

L_f represents the self-inductance of the FW, and its calculation formula is as follows:

$$L_f \approx \frac{\pi \mu_0}{2\delta k_\delta} D_i l_{ef} \lambda^*_0 N_f^2 \tag{8}$$

From (6), (7) and (8), and noting that λ^*_0 and λ^*_1 are very close, and λ^*_2 is much smaller than λ^*_0, and the winding coefficient k_N is close to 1, we get:

$$L_{f\sigma} \approx L_{md} \tag{9}$$

Further obtained:

$$L'_d \approx L_\sigma + \frac{L_{md}}{2} \tag{10}$$

In the context of the PME HIA, it is observed that the *d*-axis transient inductance of the PME HIA is equivalent to the transient inductance when the FW is open. Consequently, the transient inductance and synchronous inductance are equal. The calculation formula is presented as follows:

$$L'_{de} = L_\sigma + L_{mde} \tag{11}$$

where L'_{de} is the *d*-axis transient inductance of the PME HIA, and L_{mde} is the *d*-axis armature reaction inductance of the PME HIA. It is important to note that the *d*-axis armature reaction magnetic field of the PME HIA creates a closed loop through the PM. This configuration results in a significant MMF drop across the PM. Consequently, the equivalent per-unit value of the DC component of the air-gap permeance for the PME HIA is lower than that of the EE HIA. When calculating the transient inductance of the PME HIA using (5) and (11), it is necessary to employ the equivalent value λ^*_{e0} in (5). The calculation formula is presented as follows:

$$\lambda^*_{e0} = \lambda^*_0 - \frac{\lambda^{*2}_1 \, (1 - K_{sd})}{2\lambda^*_0} \frac{1}{2} \tag{12}$$

where K_{sd} is the magnetic flux reduction coefficient when considering the MMF drop of the PM, and when the value is 1, it means that there is no effect of the MMF drop of the PM, and when the value is 0, it means that the *d*-axis armature reaction magnetic field cannot form a closed loop through the PM. Thus, from (12), it can be seen that:

$$\lambda^*_0 > \lambda^*_{e0} > \frac{1}{2} \lambda^*_0 \tag{13}$$

From (13), it can be further obtained that the following relationship is satisfied between the *d*-axis armature reaction inductance of the PME HIA and the EE HIA:

$$L_{md} > L_{mde} > \frac{1}{2} L_{md} \tag{14}$$

Therefore, from (10), (11) and (14), it can be seen that the *d*-axis transient inductance of the PME HIA is slightly larger than that of the EE HIA.

B. q-axis Transient Inductance

For *q*-axis transient inductance, the equivalent circuit is shown in Fig. 8. The PME HIA is the same as the EE HIA, and because the *q*-axis armature reaction magnetic field does not pass through the casing and the rotating shaft to form a closed loop, the existence of PMs has no effect on the *q*-axis magnetic circuit, and the transient inductance parameters of the PME HIA and the EE HIA are equal. It is calculated as follows:

$$L'_q = L_\sigma + L_{mq} \tag{15}$$

where L_{mq} is the *q*-axis armature reaction inductance, and its

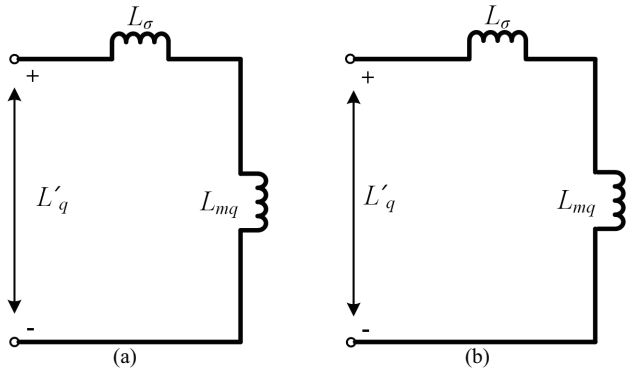

Fig. 8. The equivalent circuit for q-axis transient inductance parameters. (a) EE HIA, (b) PME HIA.

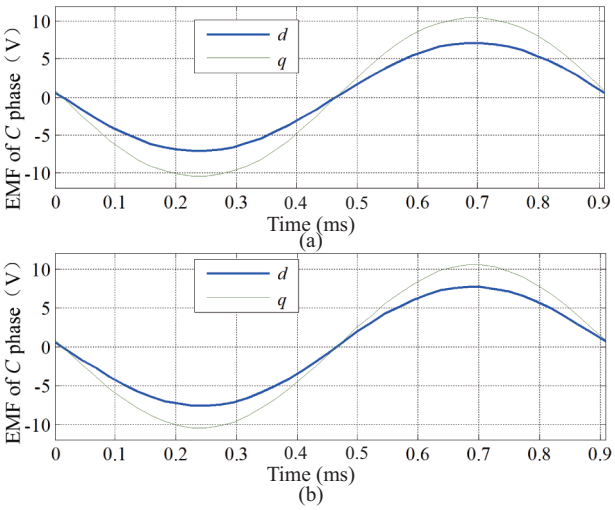

Fig. 9. C-phase EMF waveform. (a) EE HIA, (b) PME HIA.

calculation formula is as follows:

$$L_{mq} = \frac{6\mu_0 D_i l_{ef}}{\delta \pi k_\delta}\left(\frac{Nk_N}{p}\right)^2\left(\lambda^*_0 - \frac{\lambda^*_2}{2}\right) \tag{16}$$

Since λ^*_2 is much smaller than λ^*_0, there are:

$$L_{mq} \approx L_{md} \tag{17}$$

From (11), (14), (15) and (17), it can be seen that the d-axis transient inductance of the PME HIA is smaller than that of the q-axis transient inductance.

In order to validate the aforementioned conclusions, finite element simulations were employed, with the calculation methodology referenced from [30]. When the phase current amplitude is set at 100 A, the simulated EMF for the C-phase is illustrated in Fig. 9. This scenario yields transient inductances for both the d-axis and q-axis, as presented in Table II. It is evident that the d-axis transient inductance of the PME HIA is lower than that of the q-axis transient inductance, while being slightly greater than that of the EE HIA. Furthermore, the q-axis transient inductance for both the PME HIA and the EE HIA is identical. Additionally, the inductance matrix method was also utilized, with the results displayed in Table II, indicating minimal differences between the two methodologies.

V. Comparisons of Average-Value Models

A. Introduction of Derivation of AVM for CCPS Based on the EE HIA

In [17], the analytical model of a CCPS based on an EE HIA is examined. When the effects of stator resistance and the discrepancies between the d-axis and q-axis transient inductances are disregarded, the CCPS can be expressed using the following formula:

$$\boldsymbol{u}_{\mathbf{dc}} = \frac{3\sqrt{3}\omega}{\pi}\left[\psi'_d \sin(\theta_0 + \frac{\pi}{3}) + \psi'_q \cos(\theta_0 + \frac{\pi}{3})\right] - \frac{3\omega}{\pi} L_s \boldsymbol{i}_{\mathbf{dc}}\big|_{\theta_0} - 2L_s p\boldsymbol{i}_{\mathbf{dc}} \tag{18}$$

The detailed derivation of (18) is presented in Appendix B. Among them, θ_0 is the commutation delay angle, ω is the angular frequency, L_s is the equivalent internal inductance of HIA, and the equivalent inductance value is mainly related to the d-axis transient inductance value according to the analysis in [17], [19]. ψ'_d and ψ'_q are the d- and q-axis transient flux, respectively, and the calculation formula is as follows:

$$\psi'_d = \psi_f \frac{L_{md}}{L_{md} + L_{f\delta}} \tag{19}$$

$$\psi'_q = 0 \tag{20}$$

where ψ_f is the FW flux. The FW flux is determined by the following differential equation.

$$\frac{d\psi_f}{dt} = u_f - \frac{\psi_f - L_{md} i_d}{L_{md} + L_{f\delta}} r_f \tag{21}$$

where u_f and r_f are the voltage and resistance values of the FW on the stator side.

Defining:

$$u_m = \varpi \psi'_d \tag{22}$$

(18) can be further written as:

$$\boldsymbol{u}_{\mathbf{dc}} = \frac{3\sqrt{3}}{\pi} u_m \sin(\theta_0 + \frac{\pi}{3}) - \frac{3\omega}{\pi} L_s \boldsymbol{i}_{\mathbf{dc}}\big|_{\theta_0} - 2L_s p\boldsymbol{i}_{\mathbf{dc}} \tag{23}$$

As can be seen from the above equation, as shown in Fig. 10 (a), in this system, the HIA can be taken as a transient voltage connected in series with inductance.

B. Comparison of AVM for CCPS Based on the EE HIA and PME HIA

In the context of the PME HIA, and following the derivation

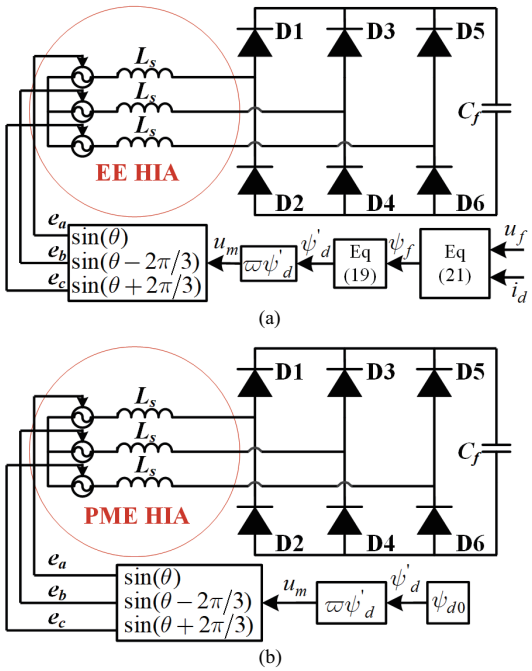

Fig. 10. Comparison of AVMs of CCPS based on PME and EE HIA. (a) EE HIA. (b) PME HIA.

presented in [17], we can disregard the effects of eddy currents within the casing and the PM, as well as the distinctions between the *d*-axis and *q*-axis transient inductances. As illustrated in Fig. 10(b), within the CCPS that utilizes the PME HIA, the PME HIA can be represented as a transient voltage that is connected in series with the *d*-axis transient inductance.

$$\psi'_d = \psi_{d0} \tag{24}$$

where ψ_{d0} represents the initial value of the *d*-axis flux, which is constant. Fig. 10 illustrates a comparison of the AVMs of the CCPS based on the PME and the EE HIA. It is evident that the PME HIA does not require consideration of the variations in transient flux, whereas the EE HIA must account for the attenuation of the transient flux.

Fig. 11 presents a comparison of the charging current and voltage waveforms derived from the 3D FEM, in conjunction with the external circuit, and the simulation results obtained from the AVM. The findings indicate that the simulation results from the AVM are largely consistent with those from the FEM. For the PME HIA, the maximum charging voltage is approximately 68 V. The AVM predicts a peak charging current of about 1420 A, whereas the finite element analysis yields a value of approximately 1720 A. This discrepancy can be attributed to the finite element simulation's incorporation of rotor eddy-current effects. Additionally, the comparison of transient flux curves is illustrated in Fig. 12. The transient flux for PME HIA remains constant, while it exhibits variability for the EE HIA. Furthermore, it is evident that for EE HIA, the simulation results that do not account for transient flux variations are greater than those that do consider these changes. Therefore, it is imperative to take transient flux variations into account for EE HIA analyses.

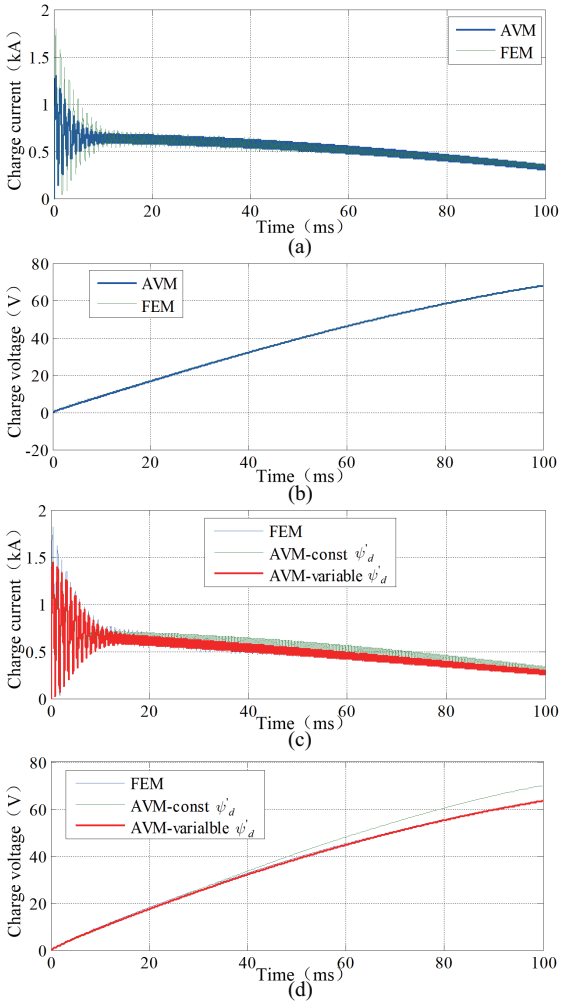

Fig. 11. Comparison of simulated waveforms between the AVM and the finite element model. (a) PME HIA charging current, (b) PME HIA charging voltage, (c) EE HIA charging current, (d) EE HIA charging voltage.

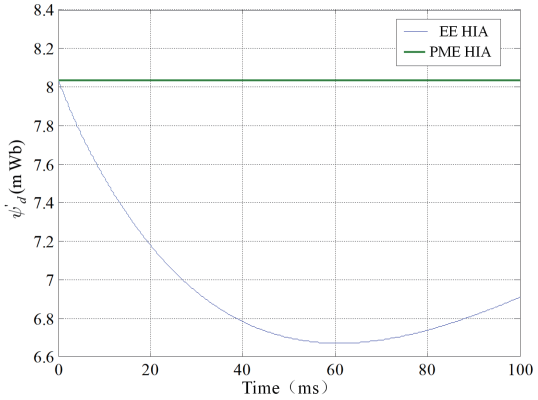

Fig. 12. Comparison of transient flux curves.

VI. Comparison of Charging Performance and Charging Efficiency

A. Comparison of Charging Performance

When the capacitance of the capacitor is 80 mF, the charging

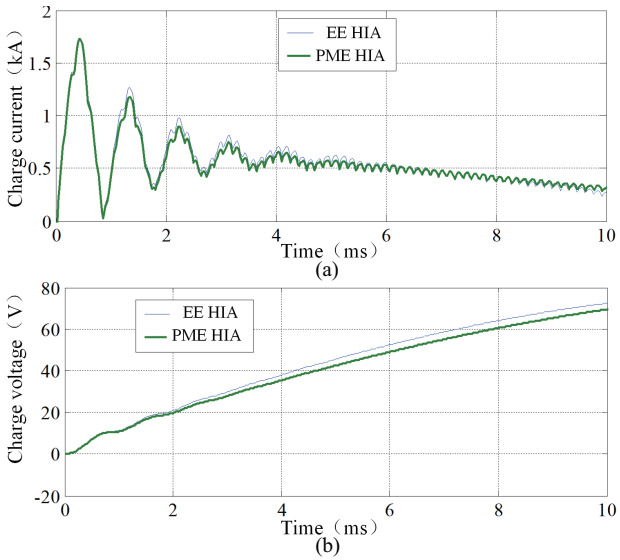

Fig. 13. Comparison of charging performance, charging time is 10 ms (capacitance 80 mF). (a) Charge current, (b) Charge voltage.

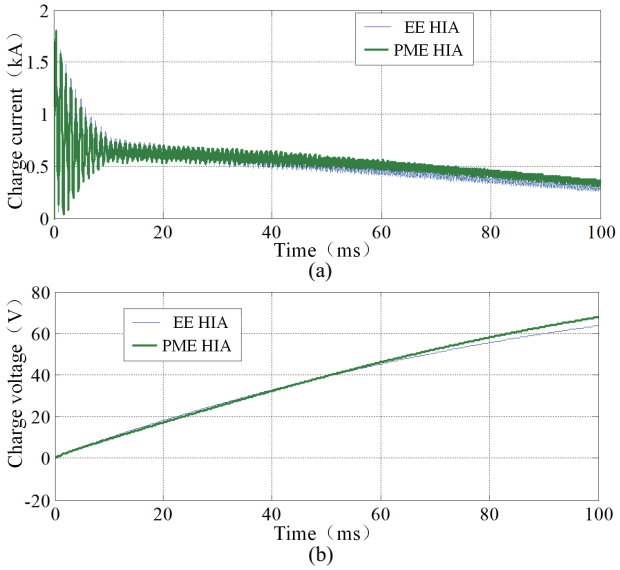

Fig. 14. Comparison of charging performance, charging time is 100 ms (Capacitance 800 mF). (a) Charge current, (b) Charge voltage.

time is recorded at 10 ms. The charging voltage and current, as determined through FEM, are illustrated in Fig. 13 for a CCPS based on a PME HIA and an EE HIA. It is evident that the *d*-axis transient inductance of the EE HIA is lower than that of the PME HIA, resulting in a slightly reduced charging current for the CCPS utilizing the PME HIA, which in turn leads to a marginally slower charging speed. The charging voltages are measured at 72.4 V for the EE HIA and 69.5 V for the PME HIA, yielding average charging powers of 21.0 kW and 19.3 kW for the EE HIA and PME HIA, respectively. Consequently, the reduction in average charging power is approximately 8%.

When the capacitance of the capacitor is 800 mF and the charging duration is 100 ms, which is nearly twice the time constant of the FW, the charging voltage and current obtained through FEM are illustrated in Fig. 14 for a CCPS based on a

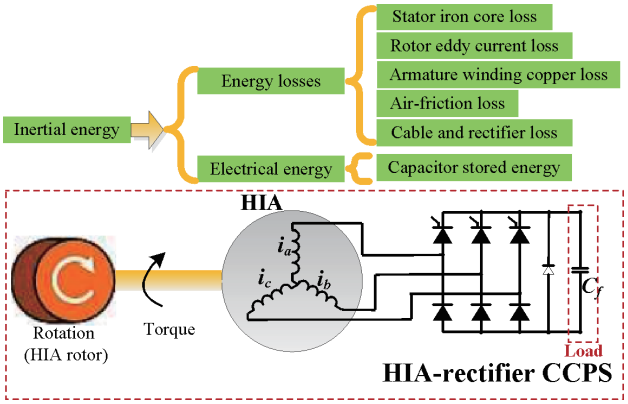

Fig. 15. The energy flow chart of CCPS based on the HIA.

PME HIA and an EE HIA. It is evident that, during extended charging times, the charging rate of the CCPS utilizing the PME HIA surpasses that of the CCPS employing the EE HIA, as the transient flux of the PME HIA remains unattenuated. The charging voltages recorded are 63.6 V for the EE HIA and 67.6 V for the PME HIA, resulting in average charging powers of 16.2 kW and 18.3 kW for the EE HIA and PME HIA, respectively. Consequently, the enhancement in average charging power is approximately 13%.

B. Comparison of Charging Efficiency

The energy flow chart of the CCPS based on the HIA is presented in Fig. 15. This analysis primarily focuses on the repeatability of the CCPS, specifically examining the conversion efficiency from the rotor's inertial energy to the electrical energy stored in the capacitor. In the case of the PME HIA, the magnetic field within the PM is DC, resulting in minimal PM losses. For the EE HIA, there is no energy exchange between the FW and the HIA rotor, thus field excitation can be disregarded. The efficiency of the CCPS based on the HIA is defined as follows: from the energy flow chart, it is evident that the charge efficiency can be calculated as the ratio of the energy stored in the capacitor to the inertial energy. The inertial energy is represented as the sum of the energy stored in the capacitor and the energy losses incurred. Therefore, the charging efficiency can be computed as outlined below:

$$\eta = \frac{E_c}{E_c + E_{loss}} \tag{25}$$

where E_c is the electrical energy on the capacitor for a single pulse, and E_{loss} is the energy loss of the CCPS. The study in [15] show that the cable and the rectifier losses are very small, so the losses on the cable and the rectifier bridge can be ignored. In the case of the switched reluctance motor (SRM), at the initial time t_{begin}, the controller for the SRM is not yet operational. Consequently, the energy supplied to the CCPS during the charging process is entirely derived from the inertial energy of the HIA rotor. So, in the calculation of efficiency, the controller of SRM needn't take into consideration.

TABLE III
THE ENERGY LOSSES FOR ONE PULSE OF 10 MS

PME HIA				
Losses	Winding copper losses	Stator iron core losses	Rotor eddy-current losses	Air-friction losses
E_{loss} (J)	38	3	0.9	0.8
E_C (J)	193			
Efficiency	81.9 %			
EE HIA				
Losses	Winding copper losses	Stator iron core losses	Rotor eddy-current losses	Air-friction losses
E_{loss} (J)	41	24	1	0.8
E_C (J)	210			
Efficiency	75.8 %			

The losses associated with the HIA comprise stator iron core losses, rotor eddy-current losses, armature winding copper losses, and air-friction losses. Simulation methodologies for various types of losses are detailed in [14] and [15]. To facilitate a comparative analysis of the efficiency of CCPS based on PME and EE HIAs, it is posited that the PME HIA is energized after 0.03 seconds—this duration corresponds to the time required for the MMR's movement—when the HIA attains its maximum operational speed. Conversely, the EE HIA is energized subsequent to the establishment of excitation. In the efficiency calculations, the initial moment is defined as the point at which the HIA reaches its peak speed, while the concluding time is marked at the completion of the charging process.

The calculated charging efficiency for the CCPS based on the PME HIA is approximately 81.9% when the charging duration is 10 ms. Table III presents the energy losses associated with each type of loss occurring during a single pulse. It is evident that copper loss constitutes the largest proportion of the total energy loss, followed by rotor eddy-current loss and stator iron core loss.

Using the PME HIA as a case study, the simulation results are presented. Fig. 16 illustrates the simulated three-phase current waveform along with its Fourier decomposition, revealing that the stator current exhibits a significant harmonic content, which consequently leads to substantial eddy-current losses in the solid rotor. Fig. 17 depicts the stator iron core loss as determined by FEM, indicating that the stator iron core loss during the charging phase is approximately equivalent to that observed under no-load conditions. Notably, when the MMR short-circuits the MMF of the PM, the stator iron core loss is markedly reduced from 100 W to approximately 5 W. Fig. 18 presents the correlation between the air-friction loss of the HIA and the rotor speed at a vacuum level of 0.8. It is evident that the air-friction loss becomes considerable when the HIA operates at high speeds, thus warranting attention in the analysis.

In the course of relocating the MMR, the amplitude of the air-gap magnetic flux density experiences a gradual increase, accompanied by a corresponding rise in the no-load iron core loss. It is assumed that the MMR moves uniformly throughout

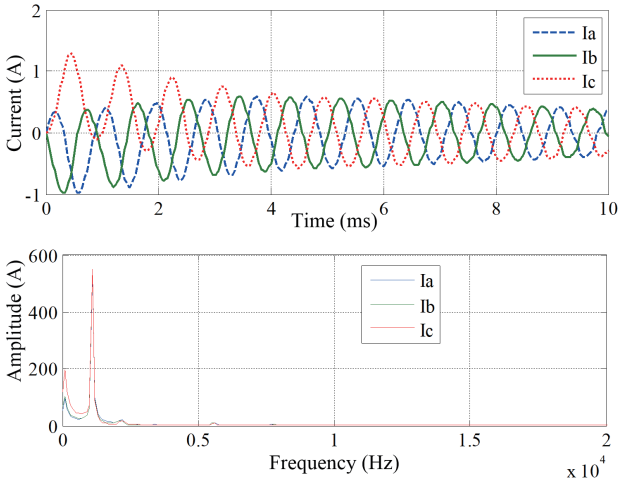

Fig. 16. Three-phase current waveform and Fourier decomposition results of finite element simulation.

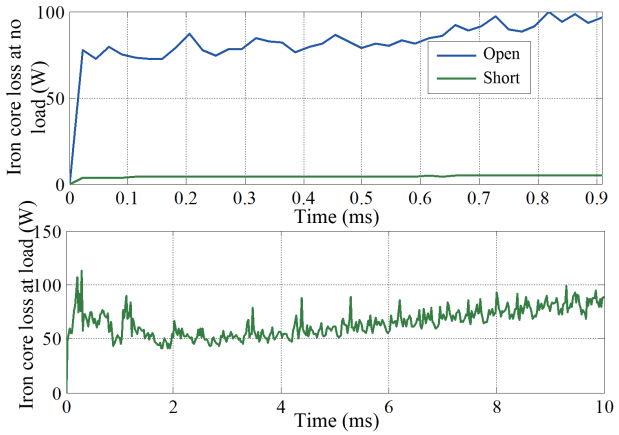

Fig. 17. Stator iron core loss for finite element simulation.

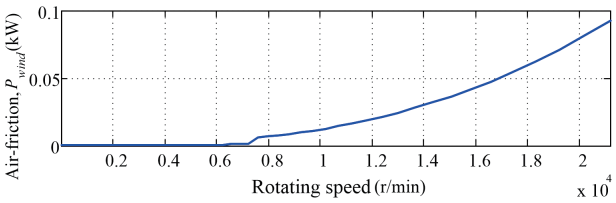

Fig. 18. Relationship between air-friction loss and rotational speed of HIA.

this process, beginning from a position aligned with the PM at time zero. At 0.03 seconds, the MMR has traversed a distance of 30 mm. Fig. 19 illustrates the temporal variations in the amplitude of the air-gap magnetic flux density, the amplitude of the armature winding flux, and the no-load iron core loss during the MMR's movement. Throughout the MMR's relocation, the energy expended due to the no-load iron core loss is quantified by integrating the time-dependent curve of the no-load iron core loss, yielding an approximate value of 2 J.

In the case of the EE HIA, the calculation of efficiency is analogous to that of the PME HIA, with the sole distinction being the inclusion of energy consumed due to the no-load iron

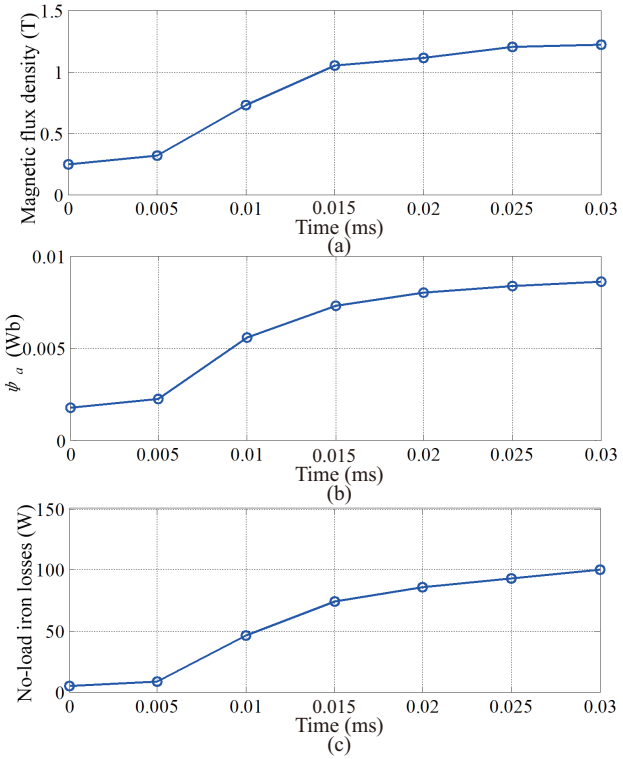

Fig. 19. Variation curves of (a) amplitude of air-gap magnetic flux density, (b) FW flux and (c) no-load iron core loss with time during the movement of the modulator.

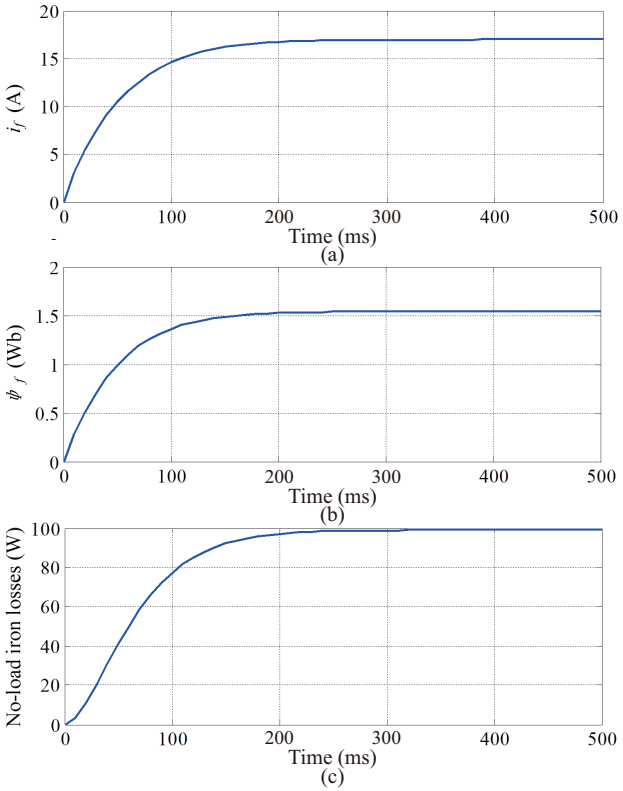

Fig. 20. Change curve of excitation establishment process. (a) Winding current, (b) flux amplitude, (c) no-load iron loss.

core loss during the excitation establishment process. Fig. 20 illustrates the FW current, FW flux, and no-load iron core loss during the excitation establishment process, as derived from FEM. The no-load iron core loss is computed using the following equation, based on the flux curve.

TABLE IV
THE ENERGY LOSSES FOR ONE PULSE OF 100 MS

PME HIA				
Losses	Winding copper losses	Stator iron core losses	Rotor eddy-current losses	Air-friction losses
E_{loss} (J)	361	12	8.5	8
E_C (J)	1833			
Efficiency	82.5 %			
EE HIA				
Losses	Winding copper losses	Stator iron core losses	Rotor eddy-current losses	Air-friction losses
E_{loss} (J)	324	33	7.7	8
E_C (J)	1651			
Efficiency	81.6 %			

$$P_{loss} = \left(\frac{\psi_f}{\psi_{f(max)}}\right)^2 P_{loss(max)} \tag{26}$$

where $\psi_{f(max)}$ and $P_{loss(max)}$ denote the FW flux and the no-load iron core loss, respectively, when the field current attains a steady state. It is observed that the time required to establish excitation for the EE HIA is approximately 0.3 seconds, which is significantly longer than that for the PME HIA. During the excitation establishment process, the energy expended due to the no-load iron core loss is quantified by integrating the time-dependent curve of the no-load iron core loss, yielding a calculated value of approximately 23 J.

It is evident from Table III that the CCPS based on PME HIA demonstrates greater efficiency than the CCPS based on EE HIA, exhibiting a 6.1% improvement in efficiency when the charge time is set at 10 ms. This increased efficiency can be attributed to the significantly longer duration required for the EE HIA to establish excitation, resulting in higher energy consumption due to no-load iron core losses. However, when the charge time is extended to 100 ms, as illustrated in Table IV, the improvement in efficiency diminishes to approximately 0.9%. This reduction in efficiency improvement is due to the fact that the energy losses associated with no-load iron core losses during the excitation establishment stage are considerably less significant at a charge time of 100 ms compared to that at 10 ms.

C. Analysis of Selection of Influence Factors on the Charge Performance and Efficiency

The analysis presented in the previous section indicates that the charging power of the CCPS based on the EE HIA is significantly influenced by the charging duration. Specifically, an increase in charging time correlates with a more pronounced effect of transient flux attenuation on the CCPS utilizing the EE HIA. Furthermore, this extended charging time also enhances the performance improvement observed when comparing the CCPS based on the PME HIA to that based on the EE HIA.

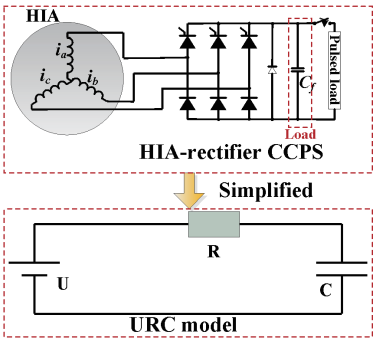

Fig. 21. The "URC" model for CCPS based on the HIA.

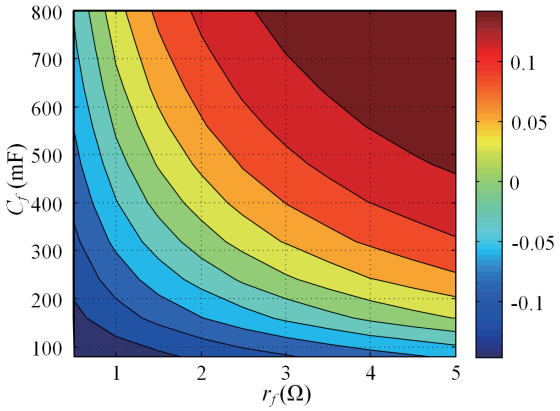

Fig. 22. The relationship between improvement of charge performance, the capacitance and FW resistance.

The simulation results presented in the previous section indicate that the enhancement of efficiency for PME HIA in comparison to EE HIA is primarily attributed to the reduction of stator iron core losses during the excitation establishment phase. It is evident that an extended charging duration results in a diminished proportion of no-load stator iron core losses relative to the total energy losses during the excitation establishment stage. Consequently, this leads to an increase in the efficiency of the CCPS and a reduction in the efficiency improvement of CCPS when utilizing PME HIA as opposed to EE HIA.

The charging performance and efficiency of the CCPS are influenced by the duration of the charging process and the FW resistance. As illustrated in Fig. 21, the HIA-rectifier CCPS can be represented as a URC circuit model, where U denotes voltage, R represents resistance (or reactance), and C signifies capacitance. To achieve optimal charging performance, the preset charging voltage is typically maintained at approximately 1.4 to 1.5 times the amplitude of the phase EMF; under these conditions, the average charging power reaches its maximum. From the URC model, it can be observed that the charging time is directly proportional to the electrical frequency, inductance, and capacitance of the capacitor. Given that the inductance is constant for a designed machine, our primary focus will be on the electrical frequency and capacitance as the key influencing factors.

D. Relationships among the Enhancement of Charge Performance, Efficiency, Capacitance, and FW Resistance

Fig. 22 illustrates the relationship between improved charge performance, capacitance, and FW resistance when the FW resistance is 0.5 Ω-5 Ω and the capacitance is 80 mF-800 mF. The charge time is proportional to the capacitance (e.g., 10 ms for 80 mF and 100 ms for 800 mF). The improvement of charge performance is defined as:

$$\Delta P = \frac{U_{\mathrm{PME}}^2 - U_{\mathrm{EE}}^2}{U_{\mathrm{EE}}^2} \tag{27}$$

where U_{PME} and U_{EE} represent the charge voltages for PME HIA and EE HIA, respectively. And it has been discovered that the higher the capacitance and FW resistance, the greater the improvement in charge performance. It has also been discovered that the equipotential line of charge performance increase is roughly an inverse proportional function, which implies that if the product of FW resistance and capacitance is a constant, the improvement in charge performance will likewise be a constant. This can be explained as follows. If the ratio of charge time to the electromagnetic time constant of HIA is const, the charge voltage will be a const. The charge time is proportional to the capacitance, and the electromagnetic time constant can be calculated by the following formula:

$$T_d' \approx \frac{L_\sigma + L_{\mathrm{f}\sigma}}{r_{\mathrm{f}}} \approx \frac{L_{\mathrm{f}0}}{2r_{\mathrm{f}0}} \tag{28}$$

where $r_{\mathrm{f}0}$ and $L_{\mathrm{f}0}$ represent the FW side's resistance and inductance, respectively. It may be discovered that the electromagnetic time constant is inversely proportional to the FW resistance. And for the parameter shown in Table II, the predicted electromagnetic time constant is around 22.5 ms. So, the ratio of charge time to the electromagnetic time constant is constant, which means that the product of FW resistance and capacitance is a constant:

$$C_{\mathrm{f}} \frac{r_{\mathrm{f}0}}{L_{\mathrm{f}0}} = \mathrm{const} \tag{29}$$

Figs. 23 and 24 show the relationship between charge efficiency, capacitance, and FW resistance for PME HIA, and EE HIA, respectively. Fig. 25 depicts the relationship between improved charge efficiency, capacitance, and FW resistance. The improvement of charge performance is defined as:

$$\Delta\eta = \frac{\eta_{\mathrm{PME}} - \eta_{\mathrm{EE}}}{\eta_{\mathrm{EE}}} \tag{30}$$

where η_{PME} and η_{EE} represent the charge efficiency for PME HIA and EE HIA, respectively. It has been discovered that for both PME HIA and EE HIA, the larger the capacitance, the higher the efficiency. This is because the higher the capacitance, the longer the charge time, and the lower the energy losses of the no-load iron core loss during the excitation estab-

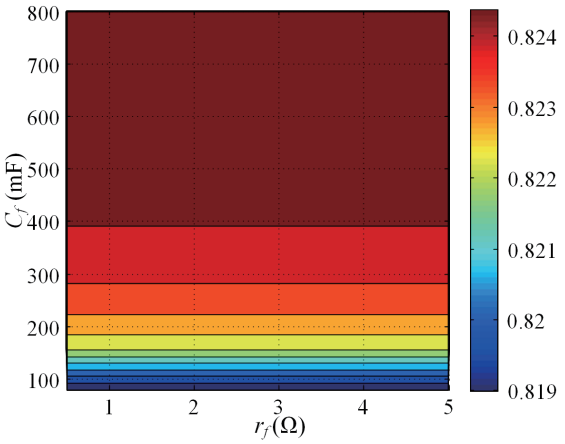

Fig. 23. The relationship between charge efficiency, the capacitance and FW resistance for PME HIA.

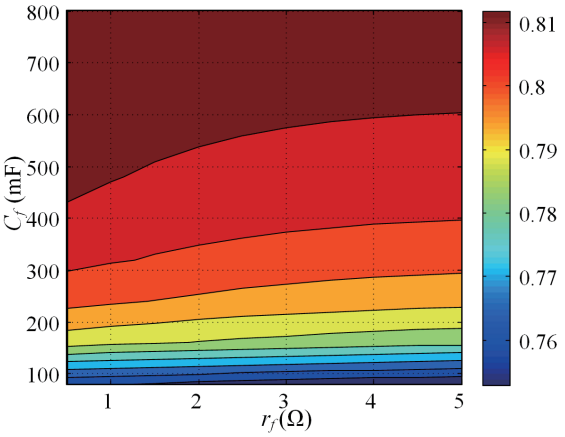

Fig. 24. The relationship between charge efficiency, the capacitance and FW resistance for EE HIA.

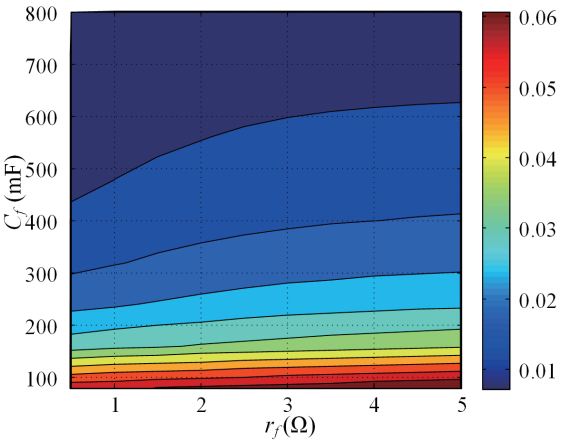

Fig. 25. The relationship between improvement of charge efficiency, the capacitance and FW resistance.

lishment stage, which account for overall energy losses. The effectiveness of PME HIA has no link with the FW resistance, because there is no FW resistance parameter. For the EE HIA, FW resistance has negligible effect on efficiency. The higher

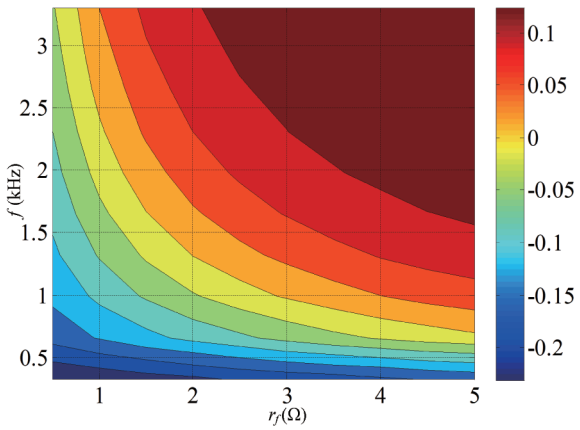

Fig. 26. The relationship between improvement of charge performance and the frequency and FW resistance.

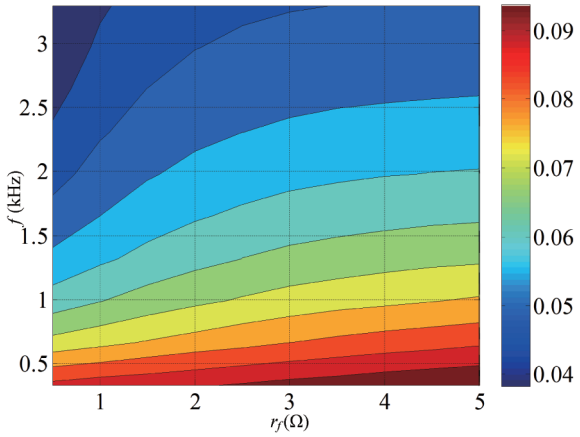

Fig. 27. The relationship between improvement of charge efficiency and the frequency and FW resistance.

the FW resistance, the lower the efficiency. This is because that, the larger the FW resistance is, the lower the charge voltage is, so the lower the energy stored in the capacitor is. The change trend for improvement of efficiency is the exact opposite with efficiency for EE HIA.

E. Relationships among the Enhancement of Charge Performance, Efficiency, Frequency, and FW Resistance

In a manner analogous to the preceding section, when the FW resistance is within the range of 0.5 Ω to 5 Ω and the electrical frequency spans from 0.367 kHz to 3.3 kHz, the relationship between the enhancement of charge performance, frequency, and FW resistance is illustrated in Fig. 26. Additionally, the relationship between the enhancement of charge efficiency, frequency, and FW resistance is depicted in Fig. 27. It is observed that the equipotential line representing the enhancement of charge performance approximates an inverse proportional function. This indicates that if the product of FW resistance and frequency remains constant, the enhancement of charge performance will also remain constant. Conversely, the trend observed for the enhancement of efficiency is in direct opposition to that of charge performance; specifically, as the

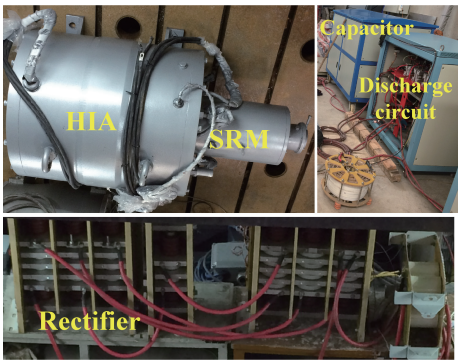

Fig. 28. Experimental system for verification of simulation models.

TABLE V
PARAMETERS OF CCPS BASED ON EE HIA FOR EXPERIMENTAL SYSTEM

Charge time	⩽35 ms
Preset charge voltage	Case 1: 4400 V Case 2: 4000 V
Rotating speed	Case 1: 8000 r/min Case 2: 6920 r/min
RMS value of line-to-line back EMF	Case 1: 3810 V Case 2: 3300 V
FW resistance	8.5 Ω
FW inductance	9.0 H
Capacitance of capacitor	7800 μF
d-axis transient inductance	0.21 mH
q-axis transient inductance	0.226 mH
Phase resistance	0.13 Ω
Moment of inertia for rotor	29 kg·m^2
Field current	18 A

TABLE VI
MAIN STRUCTURE PARAMETERS OF EE HIA FOR THE EXPERIMENTAL SYSTEM

Pole pair number	13
Rotor diameter	554 mm
Stator core inner diameter	560 mm
Stator core outer diameter	680 mm
Air-gap length	3 mm
Stator length	222 mm
Rotor slot depth	38 mm
Slot number per pole per phase	1
Armature winding series turn number per phase	26

electrical frequency increases, the enhancement of efficiency decreases.

VII. VERIFICATION OF SIMULATION MODELS BY EXPERIMENT

In order to validate the simulation model presented in the previous section, an experiment was conducted using a CCPS based on the EE HIA. The experimental setup is illustrated in Fig. 28, while the parameters pertinent to the experimental system are detailed in Table V. The key structural parameters of the EE HIA utilized in the experimental system are provided in Table VI. The transient inductances are obtained by FEM simulation, the simulation methods can be found in [31], and the

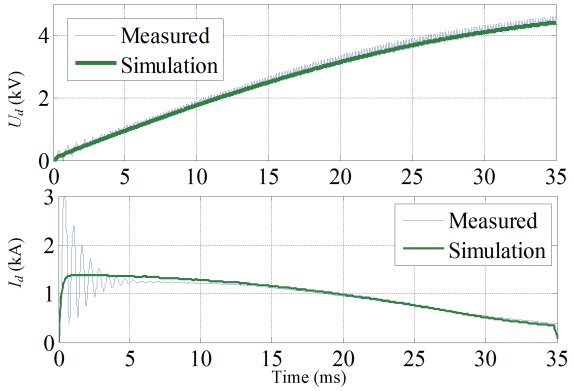

Fig. 29. The comparison of simulation and experiment results for charge current and voltage (4400 V).

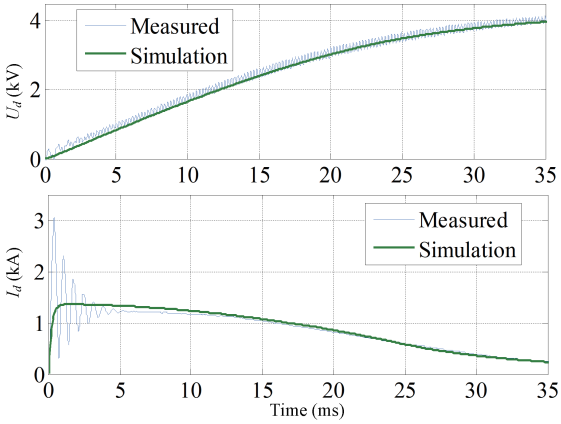

Fig. 30. The comparison of simulation and experiment results for charge current and voltage (4000 V).

magnetic saturation is also taken into consideration in this paper by applying current in the field winding. The experimental procedure is as follows: the HIA rotor is driven by a switched reluctance motor (SRM), accelerating from zero to a maximum rotational speed of approximately 8000 r/min. Subsequently, field current is applied, allowing the HIA to establish an excitation magnetic field within three seconds. Following this, the rectifier is activated, enabling the HIA to charge the capacitor through the rectifier. Once the voltage across the capacitor reaches the predetermined value, the rectifier is deactivated, resulting in the rapid discharge of the capacitor to the pulsed load. During the charging process, the waveforms of the charge current, charge voltage, and line-to-line voltage are recorded.

The comparison of simulation and experimental results for charge current and voltage is presented in Figs. 29 and 30. It can be observed that the simulation and experimental results are in strong agreement, thereby validating the AVM model discussed in the previous section.

The comparison of efficiency between simulation and experimental results for a single pulse within the experimental system is presented in Tables VII and VIII. It is evident that the results from the simulation and the experiment are in strong agreement, thereby validating the simulation model for calculating losses as discussed in the previous section. In this

TABLE VII
THE COMPARISON OF EFFICIENCY FOR SIMULATION AND EXPERIMENT FOR ONE PULSE IN THE EXPERIMENTAL SYSTEM (4400 V)

	Simulation	Experiment
Total energy losses (kJ)	18	17.7
Energy stored in the capacitor (kJ)	75.5	75.8
Efficiency	80.7%	81.0%

TABLE VIII
THE COMPARISON OF EFFICIENCY FOR SIMULATION AND EXPERIMENT FOR ONE PULSE IN THE EXPERIMENTAL SYSTEM (4000 V)

	Simulation	Experiment
Total energy losses (kJ)	14.3	14.1
Energy stored in the capacitor (kJ)	62.4	62.7
Efficiency	81.3%	81.6%

context, it is important to note that the total losses for one pulse in the experiment cannot be directly measured; instead, they are calculated as the rotor's released inertial energy minus the energy stored in the capacitor. The released inertial energy of the rotor is calculated as follows:

$$E_{\text{rotor}} = \frac{1}{2} J_{\text{rotor}} \left(\Omega^2_{\text{begin}} - \Omega^2_{\text{end}}\right) \tag{31}$$

where E_{rotor} is the rotor released inertial energy, J_{rotor} is the rotor moment of inertia, Ω_{begin} and Ω_{end} are the rotating angular speed at the beginning and end of charge process. The rotating angular speed at the beginning and end of charge process is obtained by the following formulas:

$$\Omega_{\text{begin}} = \frac{2\pi f_{\text{begin}}}{p} \tag{32}$$

$$\Omega_{\text{end}} = \frac{2\pi f_{\text{end}}}{p} \tag{33}$$

where f_{begin} and f_{end} are the electrical frequency of armature winding at the beginning and end of charge process. The electrical frequency of armature winding is obtained from the waveforms of armature winding no-load EMF.

VIII. SELECTIONS OF RATIONAL TOPOLOGICAL STRUCTURE OF CCPS

A thorough analysis is presented to determine an optimal topological structure for CCPS, specifically comparing those based on the PME HIA with those based on the EE HIA. In this study, a weighted function is employed to comprehensively assess the enhancements in charge performance and efficiency. The weighted value representing the improvement in charge performance and efficiency is defined as follows:

$$\Delta W_e = K_1 \Delta P + K_2 \Delta \eta \tag{34}$$

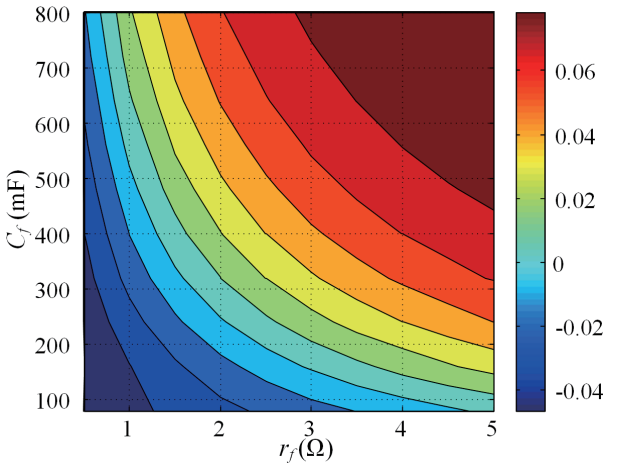

Fig. 31. The relationship between weighted improvement and the capacitance and FW resistance.

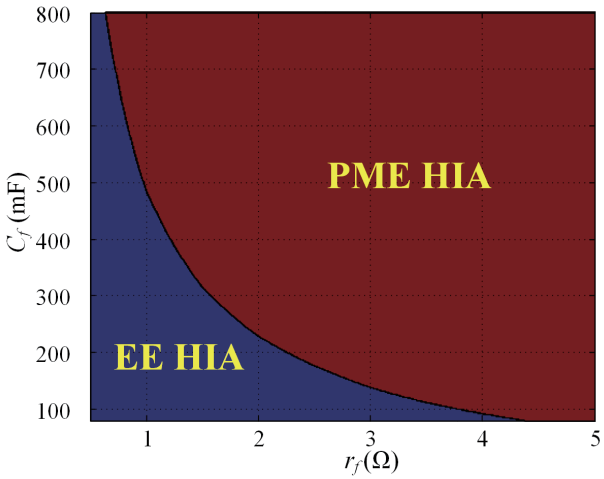

Fig. 32. The selected topological structure for CCPS with different the capacitance and FW resistance.

where K_1 and K_2 are the weighted coefficients for improvement of charge performance and efficiency respectively. Because charge performance and efficiency are equally important for the CCPS, so the coefficients for K_1 and K_2 are both chosen to be 0.5.

When K_1 = 0.5 and K_2 = 0.5, the relationship between weighted improvement, capacitance, and FW resistance is illustrated in Fig. 31. It can be observed that an increase in both capacitance and FW resistance corresponds to a greater weighted improvement. Based on the findings regarding weighted improvement, a topological structure for the CCPS can be selected according to varying capacitance and FW resistance values. The criteria for selection are as follows:

$$\begin{aligned} &if\ \Delta W_e \geqslant 0, \quad \text{select PME HIA} \\ &if\ \Delta W_e < 0, \quad \text{select EE HIA} \end{aligned} \tag{35}$$

The results presented in Fig. 32 indicate that when the production of capacitance and FW resistance is substantial, the

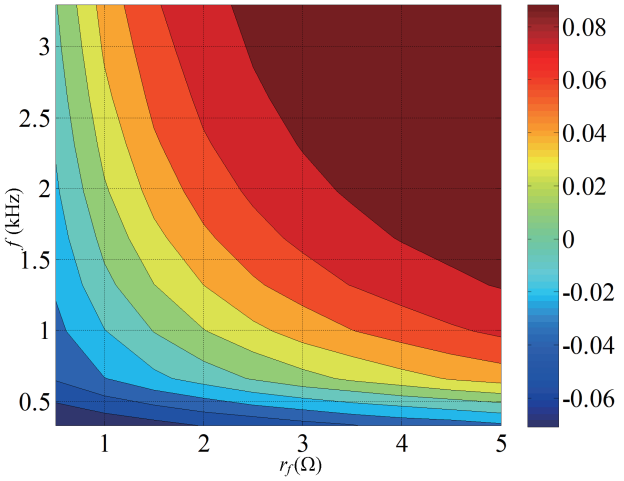

Fig. 33. The relationship between weighted improvement and the frequency and FW resistance.

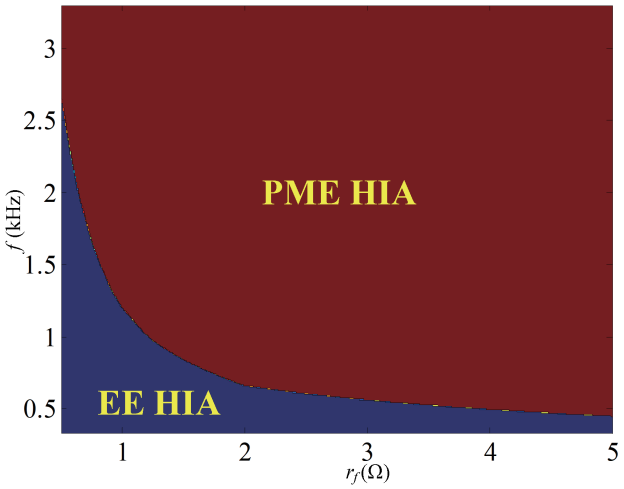

Fig. 34. The selected topological structure for CCPS with different the frequency and FW resistance.

PME HIA should be selected; conversely, if these values are not significant, the EE HIA is the appropriate choice.

The relationship between weighted improvement, frequency, and FW resistance is illustrated in Fig. 33. It is evident that an increase in both frequency and FW resistance corresponds to a greater weighted improvement. The selection outcomes between PME HIA and EE HIA are presented in Fig. 34. It can be observed that when the production of frequency and FW resistance is substantial, PME HIA is the preferred choice; conversely, EE HIA should be selected when these parameters are lower.

IX. Discussions of Advantages and Potential Limitations of PME HIA Compared with EE HIA in Practical Applications

It is important to note that while the PME HIA exhibits advantages in charge efficiency and performance, particularly in scenarios characterized by prolonged charge times and significant FW resistance, it also presents certain limitations in practical applications. For instance, in the context of electromagnetic railgun applications, the required energy storage capacity of capacitors is substantial, necessitating extended charge times. In this specific application, the charge performance of the PME HIA significantly surpasses that of the EE HIA, and the charge efficiency of the PME HIA is also superior to that of the EE HIA. However, it is crucial to acknowledge that the no-load iron core losses during idle operation for the PME HIA are greater than those for the EE HIA. This discrepancy may result in an extended duration required to accelerate the HIA rotor.

Furthermore, it should be noted that in practical applications, the structure of the MMR system with an actuator is more complex than that of the FW system with a power supply for EE HIA. This increased complexity may render the assembly and manufacturing processes of PME HIA significantly more intricate than those of EE HIA. Additionally, the control of magnetic flux regulation for PME HIA is also more complex than for EE HIA.

X. Conclusion and Future Works

A. Conclusion

In this paper, a comparative analysis of CCPS based on PME and EE HIA is conducted. The findings of this study indicate that:

(1) The amplitude of the no-load air-gap magnetic flux density for both the PME HIA and the EE HIA is equivalent. However, during idling conditions, the amplitude of the no-load air-gap magnetic flux density for the PME HIA does not diminish to zero, resulting in a residual no-load iron core loss.

(2) The *d*-axis transient inductance of the PME HIA is lower than that of the *q*-axis transient inductance and is marginally greater than the *d*-axis transient inductance of the EE HIA, which does not align with intuitive expectations. Furthermore, the *q*-axis transient inductance of the PME HIA is equivalent to that of the EE HIA.

(3) In the AVM of the CCPS based on the PME HIA, the variation of transient flux does not require consideration. Conversely, the deterioration of charging performance resulting from transient flux attenuation must be factored into the AVM of the CCPS based on the EE HIA.

(4) When the charging duration is approximately 0.45 times the electromagnetic time constant of the EE HIA, the enhancements in charging performance and efficiency are −8% and 6.1%, respectively. Conversely, when the charging duration is about 4.5 times the electromagnetic time constant of the EE HIA, the improvements in charging performance and efficiency are 13% and 0.9%, respectively.

(5) The relationships between the enhancement of charge performance, efficiency, capacitance, frequency and FW resistance have been established. It is observed that an increase in capacitance, frequency and FW resistance correlates with a greater enhancement in charge performance. The equipotential line representing the improvement in charge performance can be approximated as an inverse proportional function. This indicates that if the product of FW resistance and capacitance remains constant, or if the product of FW resistance and fre-

quency remains constant, then the enhancement in charge performance will also remain constant. Furthermore, it is noted that as capacitance or frequency increases, the improvement in efficiency diminishes.

(6) A comprehensive analysis is presented to determine an optimal topological structure for CCPS, comparing those based on the PME HIA with those based on the EE HIA. A weighted function is introduced to evaluate the overall enhancement of charge performance and efficiency. Utilizing the results of this weighted improvement, a suitable topological structure for CCPS can be identified, taking into account varying capacitance, frequency, and FW resistance. In scenarios where the product of capacitance and FW resistance, or the product of frequency and FW resistance, is substantial, the PME HIA is recommended. Conversely, the EE HIA should be employed when these products are comparatively lower.

B. Future Works

In the analysis conducted in this paper, the variation in rotor velocity during the charging process is not considered. This omission arises from the inconsistency in the charge current and voltage waveforms of each pulse, which is influenced by the reduction in no-load back EMF as the rotor velocity diminishes throughout the charging process. Consequently, the no-load back EMF of the HIA during the repeated charging process will be dynamically modified through rapid mechanical magnetic adjustments, thereby ensuring that the charge current and voltage waveforms for each pulse are as consistent as possible.

Furthermore, it is important to note that the amplitude of the no-load air-gap magnetic flux density cannot be reduced to zero, resulting in no-load iron core losses when the PME HIA is in an idle state. Consequently, this study will explore a novel type of mechanically modulated PME HIA, characterized by significantly enhanced flux weakening capability and linearity, such as the HIA featuring radially externally movable permanent magnets [32]. The objective is to achieve a reduction in the amplitude of the no-load air-gap magnetic flux density to zero during idle operation, thereby further enhancing the system's efficiency. Additionally, new topologies, including innovative magnetic-modulating structures and methods for mechanically modulated PME HIA, will be examined in detail. For instance, the investigation will focus on the mechanisms for adjusting the position of the permanent magnets in the HIA with radially externally movable permanent magnets to simultaneously achieve optimal magnetic flux regulation linearity and effective flux weakening capability.

In addition, the power density of the PME HIA is constrained due to the *d*-axis transient inductance being marginally greater than that of the EE HIA. Future research will focus on exploring methods of active compensation [23] and passive compensation [20]–[22] to enhance the transient voltage of the PME HIA and to reduce its *d*-axis transient inductance, thereby further improving the power density of the PME HIA. For the PME HIA equipped with a passive compensating winding, an in-depth investigation will be conducted on the AVM and the optimization aimed at minimizing transient inductance. For the PME HIA with an active compensating winding, the study will delve into the AVM and the optimization of compensating winding parameters, such as the number of turns. Furthermore, a comprehensive analysis of the equivalent 2D FEM model for the PME HIA, whether it incorporates a passive or active compensating winding, will also be undertaken.

A prototype of the CCPS, based on the PME HIA, will be developed in the future to validate the analyses presented in this paper.

XI. Appendix

A. Appendix A [29]

The magnetomotive force of a PM is:

$$F_{\mathrm{c}} = \frac{l_{\mathrm{m}} B_{\mathrm{m}}}{\mu_0 \mu_{\mathrm{r}}} \tag{A1}$$

where μ_0 and μ_r are the vacuum permeability and the relative permeability of the PM respectively. The magnetic resistance of a PM is:

$$R_{\mathrm{m}} = \frac{l_{\mathrm{m}}}{\mu_0 \mu_{\mathrm{r}} A_{\mathrm{shell}}} \tag{A2}$$

where A_{casing} represents the cross-sectional area of the PM, which is calculated as:

$$A_{\mathrm{shell}} = \frac{\pi}{4}(D_{\mathrm{shell}}^2 - D_o^2) \tag{A3}$$

The magnetic reluctance of the leakage circuit is:

$$R_{\mathrm{ms}} = \frac{l_{\mathrm{m}}}{A_{\mathrm{ms}} \mu_0} \tag{A4}$$

where A_{ms} represents the cross-sectional area of the magnetic leakage circuit, which is calculated as:

$$A_{\mathrm{ms}} = \frac{\pi}{4}(D_o^2 - D_{\mathrm{shaft}}^2) \tag{A5}$$

The main air-gap magnetic resistance is:

$$R_{\delta} = \frac{\delta}{A_{\delta} \mu_0} \tag{A6}$$

where A_δ represents the cross-sectional area of the main magnetic circuit, which is calculated as:

$$A_{\delta} = \pi D l \lambda_0^* \tag{A7}$$

where λ^*_0 represents the per-unit values of the DC component

of air-gap permeance. The air-gap reluctance of the modulator is:

$$R_{\delta 2} = \frac{\delta_2}{A_{\delta 2}\mu_0} \tag{A8}$$

where $A_{\delta 2}$ represents the cross-sectional area of the air gap of the modulator, which is calculated as:

$$A_{\delta 2} = \pi D_{\text{shell}} \frac{l_{\text{m}} - l_{\text{b}}}{2} \tag{A9}$$

B. Appendix B

The derivation of (18) is as follows. Since the 1/6 electrical cycle is very small relative to the electromagnetic time constant, the FWs fluxes can be regarded as in-variable, that means the transient fluxes is nearly constant. The average DC voltage is:

$$\boldsymbol{u}_{\mathbf{dc}} = \overline{u_{\text{dc}}} = \frac{3\sqrt{3}\,\omega}{\pi}\left[\psi_d \cos(\theta + \frac{\pi}{6}) - \psi_q \sin(\theta + \frac{\pi}{6})\right]\Big|_{\theta_0}^{\theta_0 + \frac{\pi}{3}} \tag{B1}$$

where θ_0 is the commutation delay angle. Assuming that the rotor fluxes are constant during one switching interval, it can be obtained that:

$$\begin{aligned} \psi_d &= -L_d^{'} i_d + \psi_d^{'} \\ \psi_q &= -L_q^{'} i_q + \psi_q^{'} \end{aligned} \tag{B2}$$

where $L_d^{'}$ and $L_q^{'}$ are both assumed to be L_{s}. Substituting (B2) into (B1), and assuming that the value of $\boldsymbol{i}_{\mathbf{dc}}$ at time of $\theta_{0+\pi/3}$ is $\boldsymbol{i}_{\mathbf{dc}}|_{\theta 0} + \Delta\boldsymbol{i}_{\mathbf{dc}}$, then (B3) can be obtained, to be:

$$\boldsymbol{u}_{\mathbf{dc}} = \overline{u_{\text{dc}}} = -\frac{3\sqrt{3}\,\omega}{\pi}\left[\psi_d^{'} \sin(\theta_0 + \frac{\pi}{3}) + \psi_q^{'} \cos(\theta_0 + \frac{\pi}{3})\right] - \frac{3\,\omega}{\pi} L_{\text{s}} \boldsymbol{i}_{\mathbf{dc}}\big|_{\theta_0} - \frac{6\,\omega}{\pi} L_{\text{s}} \Delta\boldsymbol{i}_{\mathbf{dc}} \tag{B3}$$

where $\Delta\boldsymbol{i}_{\mathbf{dc}}$ denotes the change of $\boldsymbol{i}_{\mathbf{dc}}$ during the 1/6 electrical cycle and it can be expressed as:

$$\Delta i_{\text{dc}} = \frac{\pi}{3\,\omega} p\boldsymbol{i}_{\mathbf{dc}} \tag{B4}$$

where the $\boldsymbol{u}_{\mathbf{dc}}$ and $\boldsymbol{i}_{\mathbf{dc}}$ are used as the state variable for the rectifier AVM. Substituting (B4) into (B3), the (B5) can be written as:

$$\boldsymbol{u}_{\mathbf{dc}} = -\frac{3\sqrt{3}\,\omega}{\pi}\left[\psi_d^{'} \sin(\theta_0 + \frac{\pi}{3}) + \psi_q^{'} \cos(\theta_0 + \frac{\pi}{3})\right] - \frac{3\,\omega}{\pi} L_{\text{s}} \boldsymbol{i}_{\mathbf{dc}}\big|_{\theta_0} - 2L_{\text{s}} p\boldsymbol{i}_{\mathbf{dc}} \tag{B5}$$

The $\boldsymbol{i}_{\mathbf{dc}}|_{\theta 0}$ in (B5) can be approximately expressed by the $\boldsymbol{i}_{\mathbf{dc}}$, and then the (B6) can be obtained. Here, the $i_{\text{dc}}|_{\theta 0}$ and $\overline{i_{\text{dc}}}$ are the values calculated by the (B7) and the average value of DC current, when the capacitor voltage is $\boldsymbol{u}_{\mathbf{dc}}$, respectively. The detailed derivation of commutation delay angle and the average value of DC current can be found in many related literatures [17], [19], [33], and it is omitted here due to the limited length of the paper.

$$p\boldsymbol{i}_{\mathbf{dc}} = \left[-\frac{3\sqrt{3}\,\omega}{\pi}\left[\psi_d^{'} \sin(\theta_0 + \frac{\pi}{3}) + \psi_q^{'} \cos(\theta_0 + \frac{\pi}{3})\right] - \frac{3\,\omega}{\pi} L_{\text{s}}\left[\boldsymbol{i}_{\mathbf{dc}} + i_{\text{dc}}\big|_{\theta_0} - \overline{i_{\text{dc}}}\right] - \boldsymbol{u}_{\mathbf{dc}}\right] \Big/ (2L_{\text{s}}) \tag{B6}$$

$$i_{\text{dc}}\big|_{\theta_0} = -\frac{\overline{u_{\text{dc}}}\,\frac{\pi}{3\omega} + \sqrt{3}\left[\psi_d^{'} \sin(\theta_0 + \frac{\pi}{3}) + \psi_q^{'} \cos(\theta_0 + \frac{\pi}{3})\right]}{L_{\text{s}}} \tag{B7}$$

References

[1] M. Qin, W. Chen, A. Ye, F. Zhang, S. M. Goetz, F. Yang, Z. Yu, and X. Yang, "Adaptive optimization charging strategy for LCC resonant capacitor charging power supply," in *IEEE Journal of Emerging and Selected Topics in Power Electronics*, vol. 11, no. 6, pp. 5675–5689, Dec. 2023.

[2] Y. Xu, Z. Yu, J. Chen, and Y. Wang, "A variable frequency phase-shift modulation constant power control strategy for LCC resonant capacitor charging power supply," in *IEEE Transactions on Industrial Electronics*, vol. 70, no. 2, pp. 1883–1893, Feb. 2023.

[3] A. Agarwal, Y. Prabowo, and S. Bhattacharya, "Analysis and design considerations of input parallel output series-phase shifted full bridge converter for a high-voltage capacitor charging power supply," in *2021 IEEE 12th Energy Conversion Congress & Exposition - Asia (ECCE-Asia)*, Singapore, 2021, pp. 1068–1075.

[4] J. Chen, Y. Xu, H. Lu, Z. Yan, Z. Yu, Q. Li, and Y. Tan, "Fixed frequency LCC resonant converter modeling and optimal design for high-voltage capacitor charging power supply in constant power control," in *IEEE Transactions on Industry Applications*, vol. 59, no. 4, pp. 4287–4299, Jul.-Aug. 2023.

[5] H. S. Grover and F. Dawson, "A new hybrid pulsed power circuit topology for gas laser applications," in *IEEE Transactions on Plasma Science*, vol. 49, no. 10, pp. 3181–3188, Oct. 2021.

[6] P. Zhang, H. Li, B. Zhao, Z. Wang, F. Liu, and C. Hu, "A capacitive pulsed power supply circuit with ICCOS technique for reluctance coil launchers," in *IEEE Transactions on Plasma Science*, vol. 51, no. 12, pp. 3640–3646, Dec. 2023.

[7] J. Zhao, H. Li, B. Zhao, J. Liu, L. Kong, and P. Zhang, "An improved pulsed power supply circuit for reluctance electromagnetic launcher based on bridge-type capacitor circuit," in *IEEE Transactions on Plasma Science*, vol. 51, no. 5, pp. 1351–1356, May 2023.

[8] C. -H. Kwon, J. -S. Bae, T. -H. Kim, S. -H. Son, S. -R. Jang, C. -H. Yu, S. -K. Ahn, and H. -S. Kim, "15-kV and 1.8-kJ/s high-precision capacitor charging power supply based on LCC resonant converter for kicker modulator system," in *IEEE Transactions on Plasma Science*, vol. 51, no. 10, pp. 2841–2848, Oct. 2023.

[9] S. -H. Son, C. -H. Kwon, T. -H. Kim, C. -H. Yu, S. -R. Jang, S. -T. Han, J. -S. Kim, C. -H. Cho, and H. -S. Kim, "Development of 120 kV and 60 kW three phase LCC resonant converter for electron beam welding system," in *IEEE Transactions on Plasma Science*, vol. 51, no. 10, pp. 2813–2822, Oct. 2023.

[10] Z. Ren, K. Yu, Q. Xin, and Y. Pan, "Performance of homopolar inductor alternator with diode-bridge rectifier and capacitive load," in *IEEE*

Transactions on Industrial Electronics, vol. 60, no. 11, pp. 4891–4902, Nov. 2013.

[11] Q. Xin, K. Yu, Z. -A. Ren, Z. Lou, and C. Ye, "Inductance mathematic model of a homopolar inductor alternator in a novel pulse capacitor charge power supply," in *IEEE Transactions on Plasma Science*, vol. 41, no. 5, pp. 1231–1236, May 2013.

[12] C. Ye, K. Yu, W. Xu, and H. Zhang, "Optimal design and experimental research of a capacitor-charging pulsed alternator," in *IEEE Transactions on Energy Conversion*, vol. 30, no. 3, pp. 948–956, Sept. 2015.

[13] Q. Xin, K. Yu, Q. You, and M. Yuan, "Repetition pulse charging characteristics for homopolar inductor alternator with rectified capacitive load", in *IEEJ Transactions on Electrical and Electronic Engineering*, vol. 10, no. 1, pp. 44–49, Jan. 2015.

[14] K. Yu, L. Liu, and X. Xie, "Design consideration of eddy-current loss for rotor of HIA with rectifier and capacitive loads," in *IEEE Transactions on Plasma Science*, vol. 46, no. 8, pp. 2949–2953, Aug. 2018.

[15] L. Liu, K. Yu, and X. Xie, "Analysis and test efficiency of a high-power pulsed power pupply based on HIA," in *IEEE Transactions on Plasma Science*, vol. 47, no. 5, pp. 2293–2301, May 2019.

[16] S. Guo, K. Yu, L. Jiang, P. Liu, Y. Tong, Q. Zhang, C. Xia, C. Sun, and X. Xie, "Optimization of design method and experiment of a repetition pulse charging HIA-CCPS," in *IEEE Transactions on Industry Applications*, vol. 59, no. 1, pp. 745–758, Jan.-Feb. 2023.

[17] Z. Yi, K. Yu, H. Lai, S. Guo, and X. Xie, "Average-value modeling of a capacitor charge power supply with homopolar inductor alternator," in *2022 IEEE 3rd China International Youth Conference on Electrical Engineering (CIYCEE)*, Wuhan, China, 2022, pp. 1–7.

[18] S. Guo, K. Yu, Z. Yi, J. Wang, X. Xie, and J. Yao, "An improved simplified model of capacitor charging power supply with homopolar inductor alternator considering field flux linkage and speed changes," in *2023 IEEE 6th International Electrical and Energy Conference (CIEEC)*, Hefei, China, 2023, pp. 1151–1155.

[19] K. Yu, J. Yao, S. Guo, and X. Xie, "Study of capacitor charge power supply with homopolar inductor alternator: System modelling and mode analysis," in *IET Power Electronics*, vol. 14, no. 1, pp. 14–26, Jan. 2021.

[20] K. Yu, J. Yao, X. Xie, and P. Tang, "Analysis of a novel excitation compensated homopolar inductor alternator used for capacitor charge power supply," in *IEEE Transactions on Plasma Science*, vol. 47, no. 11, pp. 5165–5171, Nov. 2019.

[21] J. Yang, C. Ye, X. Liang, and F. Xiong, "Study of a novel high-speed compensated pulsed alternator with multistage stator cores," in *IEEE Transactions on Plasma Science*, vol. 47, no. 5, pp. 2376–2381, May 2019.

[22] S. Guo, K. Yu, Z. Yi, and X. Xie, "Research on homopolar inductor alternator with a short-circuit compensated winding in CCPS system," in *IEEE Transactions on Plasma Science*, vol. 51, no. 9, pp. 2676–2687, Sept. 2023.

[23] S. Guo, K. Yu, Z. Yi, H. Lai, and X. Xie, "Analysis and experiment of homopolar inductor alternator with an active compensated winding in capacitor charging power supply system," in *IEEE Transactions on Industry Applications*, vol. 60, no. 2, pp. 2517–2531, Mar.-Apr. 2024.

[24] L. Liu, K. Yu, and X. Xie, "A high-temperature superconducting homopolar inductor alternator with slotless stator core for high-power pulsed power supply," in *2023 IEEE International Conference on Power Science and Technology (ICPST)*, Kunming, China, 2023, pp. 151–156.

[25] J. Yang, Q. Li, C. Deng, X. Qi, C. Ye, J. Yi, and S. Huang, "Investigation on the method for reducing the time constant of exciting winding of homopolar inductor machine," in *IEEE Transactions on Transportation Electrification*, vol. 9, no. 2, pp. 3255–3267, Jun. 2023.

[26] L. Liu, K. Yu, X. Xie, Z. Liu, and C. Guo, "Analysis of repetition capacitor charge system based on permanent magnet excited homopolar inductor alternator," in *The Proceedings of the 18th Annual Conference of China Electrotechnical Society*, Nanchang, China, 2023, pp. 200-206.

[27] Q. Li, J. Yang, S. Huang, P. Liu, Y. Feng, and L. Wang, "No-load electromagnetic performance analysis of a mechanically modulated permanent magnet homopolar inductor machine," in *IEEE Transactions on Transportation Electrification*, vol. 8, no. 1, pp. 1168–1181, Mar. 2022.

[28] J. Yang, Q. Li, S. Huang, C. Ye, P. Liu, B. Ma, and L. Wang, "Design and analysis of a novel permanent magnet homopolar inductor machine with mechanical flux modulator for flywheel energy storage system," in *IEEE Transactions on Industrial Electronics*, vol. 69, no. 8, pp. 7744–7755, Aug. 2022.

[29] L. Liu, K. Yu, and X. Xie, "Optimization method for minimum mass of permanent magnet excited HIA with air-gap winding," in *2023 IEEE International Conference on Power Science and Technology (ICPST)*, Kunming, China, 2023, pp. 1-6.

[30] K. Yu, L. Jiang, S. Guo, C. Xi, and X. Xie, "An optimized design method of homopolar inductor alternator based on genetic algorithm," in *IEEE Transactions on Plasma Science*, vol. 51, no. 2, pp. 544–552, Feb. 2023.

[31] Z. Lou, Y. Cheng, Y. He, Q. Shen, X. Xie, and K. Yu, "Analytical calculation of synchronous reactances of homopolar inductor alternator," in *IEEE Transactions on Plasma Science*, vol. 43, no. 5, pp. 1462–1468, May 2015.

[32] L. Liu, K. Yu, X. Xie, Z. Liu, C. Guo, M. Zhang, B. Rao, and X. Sun, "Electromagnetic performance analysis of homopolar inductor alternator with radial externally movable permanent magnets," in *The Proceedings of the 18th Annual Conference of China Electrotechnical Society*, Nanchang, China, 2023, pp. 503-509.

[33] S. D. Sudhoff, K. A. Corzine, H. J. Hegner, and D. E. Delisle, "Transient and dynamic average-value modeling of synchronous machine fed load-commutated converters," in *IEEE Transactions on Energy Conversion*, vol. 11, no. 3, pp. 508–514, Sept. 1996.

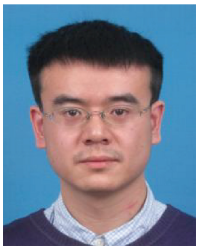

Longjian Liu was born in China, in 1989. He received the B.E. degree and Ph.D. degree in electrical engineering from the Huazhong University of Science and Technology (HUST), Wuhan, China, in 2013, and 2019, respectively. He is currently a Lecturer with the Kunming University of Science and Technology (KUST). His current research interests include electrical machinery.

Kexun Yu received the B.E., M.E., and Ph.D. degrees in electrical engineering from HUST, Wuhan, China, in 1982, 1985, and 1989, respectively. He is currently a Professor with the HUST. His current research interests include high performance electric drive systems and optimization design of electromagnetic devices.

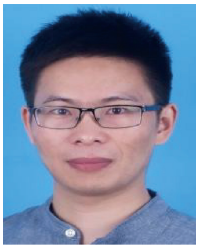

Xianfei Xie was born in China, in 1988. He received the B.E. degree and Ph.D. degrees in electrical engineering from the HUST, China, in 2011, and 2016, respectively. He is currently an Associate Professor with the HUST. His current research interests include electrical machinery and drives and design of power electronics.

Zhijian Liu was born in China, in 1975. He received the Ph.D. degrees in Electric Power System and Automation from the Harbin Institute of Technology, China, in 2010. He is currently a Professor with the KUST. His current research interests include power system.